Mangrove zonation mapping in West Africa, at 10-m resolution, optimized for inter-annual monitoring

Florent Lombard, Safietou Soumaré, Julien Andrieu, Didier Josselin

Mangrove zonation mapping in West Africa, at 10-meter resolution, optimized for inter-annual monitoring

Florent Lombard[a], Safietou Soumaré[a,b], Julien Andrieu[a,c], Didier Josselin[d]

[a] *Department of Geography, Université Côte d'Azur, CNRS UMR Espace Campus Valrose, Bâtiment L 28, avenue de Valrose 06108 Nice Cedex 2 France*

[b] *Laboratoire des Sciences et Techniques de l'Eau et de l'Environnement (LaSTEE) - Ecole Polytechnique de Thiès, BP A10 THIÈS, Senegal*

[c] *Department of Geomatics, French Institute of Pondicherry (IFP) UMIFRE 21 CNRS-MEAE / UAR 3330 11, St. Louis Street, P.B. 33 Pondicherry, 605001, India*

[d] *CNRS UMR Espace, 74 rue Louis Pasteur, 84029 Avignon CEDEX, France*

florent.lombard@univ-cotedazur.fr

Mangrove zonation mapping in West Africa, at 10-meter resolution, optimized for inter-annual monitoring

The surface area of mangrove ecosystems in Senegal have fluctuated substantially over several decades. Satellite data at 10 to 30-meter resolution, which has been available since the 1980s, has allowed the mapping and quantification of these dynamics. However, the plant formations have reorganized internally; this has not been well-documented, possibly because there is no established method for detecting zonation of the Senegalese mangrove. This paper proposes a two-step method for mapping the zonation of the Saloum Delta mangrove. First, mangrove surfaces were detected using machine learning methods from an object-based time series. Finally, a typology was developed through object-based clustering using time-series metrics derived from the harmonic regression modelling of the vegetation fraction. A comparison with field data allowed us to determine the number of classes and discriminating variables. The results showed that the selected method resulted in an overall accuracy of 97.55% (Kappa = 95.42) for the land cover at 4 classes (Water, Mangrove, Salt flats, Other land covers), with an F1-Score of 98.91% for the mangroves. Second, our results suggest that the annual trend of the vegetation fraction at the object scale is effective in differentiating mangrove zonation into three classes based on canopy density and stand height (HM: High mangrove; LDM: Low and dense mangrove; LOM: Low and open mangrove). Finally, the temporal stability of the classes and uncertainty around the magnitudes of the plant fraction values per class were assessed by Bayesian inference. An overall accuracy of 85.5% can be expected to identify the zonation typology on an inter-annual scale. This mapping technique can be used to characterize the rate of change in zonation in response to environmental changes and to guide management strategies.

Key policy highlights

- There is currently no method for detecting the zonation of the Senegalese mangrove.
- A typology of mangrove zonation was created based on canopy density and stand height.
- Analyzed temporal stability/uncertainty by time series synthesis & Bayesian modeling.
- Accurately identified typology (85.5% accuracy) in annual monitoring context
- Reduced uncertainty margins for monitoring using temporal segmentation algorithms.

Keywords: Mangrove; Sentinel-2; Sentinel-1; Times series; Machine Learning; OBIA

1. Introduction

Mangrove mapping is an important aspect of ecosystem management strategies (Giri et al., 2011). The availability of remotely sensed megadata at decametric spatial resolution allows the classification of different surface states over large continental areas (Mutanga and Kumar, 2019), especially at a scale that can guide local and national environmental policies. Access to and processing of Landsat and Sentinel archives have been facilitated by freely available cloud platforms, such as the Google Earth Engine (GEE) (Alonso et al., 2016; Gorelick et al., 2017; Wang et al., 2019). Furthermore, the computational power allocated by these platforms provides an opportunity for tropical countries to set up complex processing chains with big data (Midekisa et al., 2017). However, their dimensionality remains an important issue with regards to reducing computation times, which decreases the redundancy of information from different sensors (Myint et al., 2011; Hu et al., 2019; Stromann et al., 2020) and ensures classification efficiency (Speiser et al., 2019). Moreover, the Sahelo-Sudanese coastal zone contains socio-ecosystems that generate a variety of landscapes (Temudo et al., 2015; Andrieu, 2020) that can be difficult to map (Cabral and Costa, 2017; Asenso Barnieh et al., 2020) and which can cause spectral confusion between the mangrove and dense forests on dry land depending on the season. Therefore, extracting the most effective data and variables is essential (Schulz et al., 2021).

Mangrove forests cover large areas (Cabral and Costa, 2017; Andrieu, 2018) and provide various ecosystem services (Cormier-Salem, 1999; Walters et al., 2008; Mukherjee et al., 2014; Arumugam et al., 2021). Global issues of climate change mitigation through carbon sequestration and preservation of mangrove biodiversity must be considered alongside local issues such as access to resources (Cormier-Salem et Panfili, 2016). Monitoring mangrove dynamics on a regular basis could help better reconcile resource management within changing environments.

Mapping mangrove ecosystems in West Africa is crucial for developing effective ecosystem management strategies (Jia et al., 2018). With the help of high resolution satellite data from Landsat and Sentinel, as well as access to cloud platforms such as Google Earth Engine (GEE) (Alonso et al., 2016; Gorelick et al., 2017; Wang et al., 2019), it is now possible to use powerful computing resources and advanced processing methods to better understand the dynamics of mangroves in this region (Midekisa et al., 2017). These methods allow for the management of long and dense time series data, which can provide a comprehensive view of mangrove ecosystems. The mapping of mangroves in West Africa is particularly valuable due to the numerous ecosystem services they provide (Cormier-Salem, 1999; Walters et al., 2008; Mukherjee et al., 2014; Arumugam et al., 2021).

Although databases of mangrove areas exist (GWM, 2010; USGS, 2014), they are highly inaccurate, particularly in West Africa due to persistent cloud cover (Bunting et al., 2018). The authors also mention that fringing and fragmented mangroves are sometimes omitted, even though they are frequently encountered in West-Africa (Liu et al., 2021). Mapping the extent of mangroves has been the subject of many studies (Kuenzer et al., 2011; Wang et al., 2019), and various mapping methods have been developed to produce local data. SPOT data has successfully mapped the extent of mangroves in West Africa over several years with an object-based image analysis (OBIA) approach (Conchedda et al., 2008). Landsat data has also led to the production of accurate maps using a pixel approach combined with linear spectral unmixing (Han et al., 2018). These data are also advantageous due to the long time

series. Cloud cover has often been mentioned as an impediment to mapping mangroves in the tropics with passive sensors (Kuenzer et al., 2011); active sensors are therefore of interest for mapping mangrove surfaces. These data also present good precision scores, especially with OBIA approaches (Flores de Santiago et al., 2013), and most of these methods are fairly accurate, particularly with Sentinel-2 optical data (Mondal et al., 2019) and Sentinel-1 and 2 radar-optical combinations (Liu et al., 2021). These data have the advantage of being freely accessible and easily available on GEE. Machine learning approaches, which typically combine a large volume of data to avoid the biases of single-date image-based mapping (Cardenas et al., 2017), are currently favored for map development (Chen et al., 2017; Mondal et al., 2019; Liu et al., 2021; Wang et al., 2018). Several studies have highlighted the contributions of cloud solutions, such as GEE, for processing time series and multi-source data (Cardenas et al., 2017; Chen et al., 2017; Liu et al., 2021; Xiao et al., 2021). Combining optical (Landat-8 and Sentinel-2) and radar (Sentinel-1) data was found to improve the discrimination of Land Use Land Cover and mangrove classes (Clerici et al., 2017; Zhao and Qin, 2020; Xiao et al., 2021). Decision trees, such as Classification And Regression Trees (CART) or Random Forests (RF) are commonly used for mangroves (Giri et al., 2015; Zhang et al., 2017; Mondal et al., 2019; Thomas et al., 2018; Chen et al., 2020; Xiao et al., 2021). Liu et al. (2021) combined three algorithms with a gradient boosting machine (GBM) and neural network (NN) to form a powerful machine learning package. They achieved accuracy scores above 95% using S2 and S1 images in West Africa, and developed the most accurate mapping for this area to date.

Although the available mapping of mangrove areas seems reliable, differentiating between the mangrove plant formations using optical and radar data is challenging in West Africa (Flores de Santiago et al., 2013). Indeed, these can be characterized by the coverage and stand height, and by estimating the specific species compositions. Thus, plant formations roughly represent the zonation of mangroves and the resultant spatial organization of population dynamics at the local scale.

Subdivision of mangroves into several facies at a decametric resolution is a complex process; although it has been performed in other mangrove areas, it has rarely been attempted in Senegal. Various approaches have been developed to subdivide mangroves. The OBIA method consistently achieves good scores (Wang et al., 2019). Myint et al. (2008) mapped mangroves at a specific level using Landsat images with an overall accuracy of 94.2% and a kappa coefficient of 0.91; the pixel classifiers had an overall accuracy of 62.8% and a kappa coefficient of 0.57. Wang et al. (2018) achieved an overall accuracy of 70.95% for species community discrimination using S2 images with a combination of the object approach and an Random Forest (RF) classifier. In addition, approaches using pixel-level mangrove phenology have been used to classify mangroves at specific levels (Bullock et al., 2017; Valderrama-Landeros et al., 2021). Vegetation indices from dense S2 time series also made it possible to classify mangroves according to a three-class typology (*Rhizophora mangle* fringe, basin, and *Avicennia germinans* shrub) with overall accuracy scores between 92 and 95% (Vizcaya-Martínez et al. 2022). The authors were able to map the evolution of this typology after disturbances and measured species recovery, which are similar to those of the mangroves in Senegal. Finally, linear spectral unmixing consistently shows good results for quantifying mangrove canopy cover (Monsef and Smith, 2017; Bullock et al., 2020; Lymburner et al., 2020) and for establishing a forest composition typology (Gudex-Cross et al., 2017). For example, linear spectral unmixing was used to establish a 3-class typology in Australia (woodland, open forest, closed forest) based on the mangrove cover rate from Global Mangrove

Watch (GMW) data (Lymburner et al., 2020. Finally, several studies have used RADAR data to map mangrove species (Flores de Santiago et al., 2013; Ghazali et WIkantika, 2021). Although RADAR data has shown good accuracy in discriminating mangrove, the species classification remains more delicate and obtains low (OA = 26%) to moderate (OA ≈ 65%) scores. The best scores were obtained by optimizing the scale parameter with an OBIA approach (Flores de Santiago et al., 2013) or by deriving a dual-polarity RADAR vegetation index (DpRVI) with Sentinel-1 (Ghazali et WIkantika, 2021).

Furthermore, significant fluctuation in mangrove forest area in West Africa has occurred in recent decades (Andrieu, 2018). Mangroves in Senegal have experienced surface regeneration since the mid-1990s (Conchedda et al., 2011; Dièye et al., 2013; Andrieu, 2018; Fent et al., 2019; Lombard and Andrieu, 2021). However, the respective shares of species in regeneration processes differ according to the hydrosystems (Andrieu et al., 2020; Lombard et al., 2020). Therefore, a map of plant formation is important to obtain an overview of mangrove composition and to understand mangrove resilience to environmental changes. Plant formations can estimate the specific composition of the environment, the density of the cover, and the size of the individuals making up the group. Moreover, as was pointed out by Wang et al. (2019), mapping mangrove communities is important for conservation strategies (Jia et al., 2018). We assume that fine-scale processes participate in the spatial organization of mangrove zonation. The establishment of propagules of different species is constrained by environmental variables such as salinity and hydroperiod (Krauss et al., 2008) or sedimentary processes (Balke et al., 2013). In addition, propagule establishment has been reorganized in the face of recent environmental fluctuations in Senegal (Lombard et al, 2020). Therefore, our objective is to be able to map mangrove zonation, leading to an understanding of the arrangement of species zonation resulting from reproduction and growth, which are processes sensitive to environmental fluctuations. Therefore, our objective was to develop an optimized and robust multilevel mapping method for mangrove plant formations in the Sahelo-Sudanese delta.

By utilizing the knowledge gained from the different approaches mentioned above, we developed a method for mapping mangroves at two levels. First, mangrove surfaces were detected by machine learning of objects and corrected by classification based on linear spectral unmixing. Second, linear spectral unmixing was reapplied to subdivide the mangroves into several plant formations using the OBIA method and classified based on a 1-year time series.

2. Study areas and data

2.1.Study site

The study area (Fig. 1) covers the Saloum Delta hydrosystem. Located in the Sahelo-Sudanian domain, the north-south gradient is characterized by important inter-annual rainfall variations (Nicholson, 2013; Descroix et al., 2015); mangroves develop under a rainfall of 560 mm in the north and 800 mm in the south (Lombard et al., 2020). The forest comprises six species (*Avicennia germinans, Conocarpus erectus, Laguncularia racemosa, Rhizophora racemosa, Rhizophora mangle, Rhizophora harisonnii*) but three dominate almost the mangrove forest: *Rhizophora racemosa*, *Rhizophora mangle*, and *Avicennia germinans* (Sow et al., 1991; Ndour et al., 2012; Andrieu et al., 2020; Lombard et al., 2020). Species composition, in addition to vegetation cover and tree height, is spatially structured in zonation, and can be subdivided into plant formations. Mangroves in Senegal and Guinea-Bissau have the same zonation patterns

(Sow et al., 1991), but the studied hydrosystem showed unique features. In the Saloum Delta (and the Casamance Estuary), the salinity increases from downstream to upstream (Barusseau et al., 1985; Descroix et al., 2020), whereas the estuaries of Gambia and those located in Guinea-Bissau, for example, have a river input and upstream salinity levels closer to those of fresh water. For Saloum, this results in hypersalinity of the water even after the rainy season (Diop, 1997). The salinity of the water throughout the Saloum Delta was higher than that of the sea. For example, in Sine-Saloum in June, salinity is approximately 35‰ at the mouth of the delta and up to 100‰ in Fatick (82 km from the mouth) (Descroix, 2018). Mangrove ecosystems in coastal areas are affected by their interplay of soil, topography, and salinity, which bring complexity to the fine scale. (Marius, 1985; Diop, 1990). In such an ecological context, the vegetation shows two gradients, north–south and east–west, where the density and height of the stands differ without changing the specific composition. This makes detecting species and plant formations within the Saloum Delta challenging. Therefore, sixty fields surveys were conducted (Figure 1). Using transects following the protocol developed by Andrieu et al. (2020), the density of the vegetation cover, height of individuals, and rate of cover of each species were inventoried, which facilitated the evaluation of vegetation formation maps.

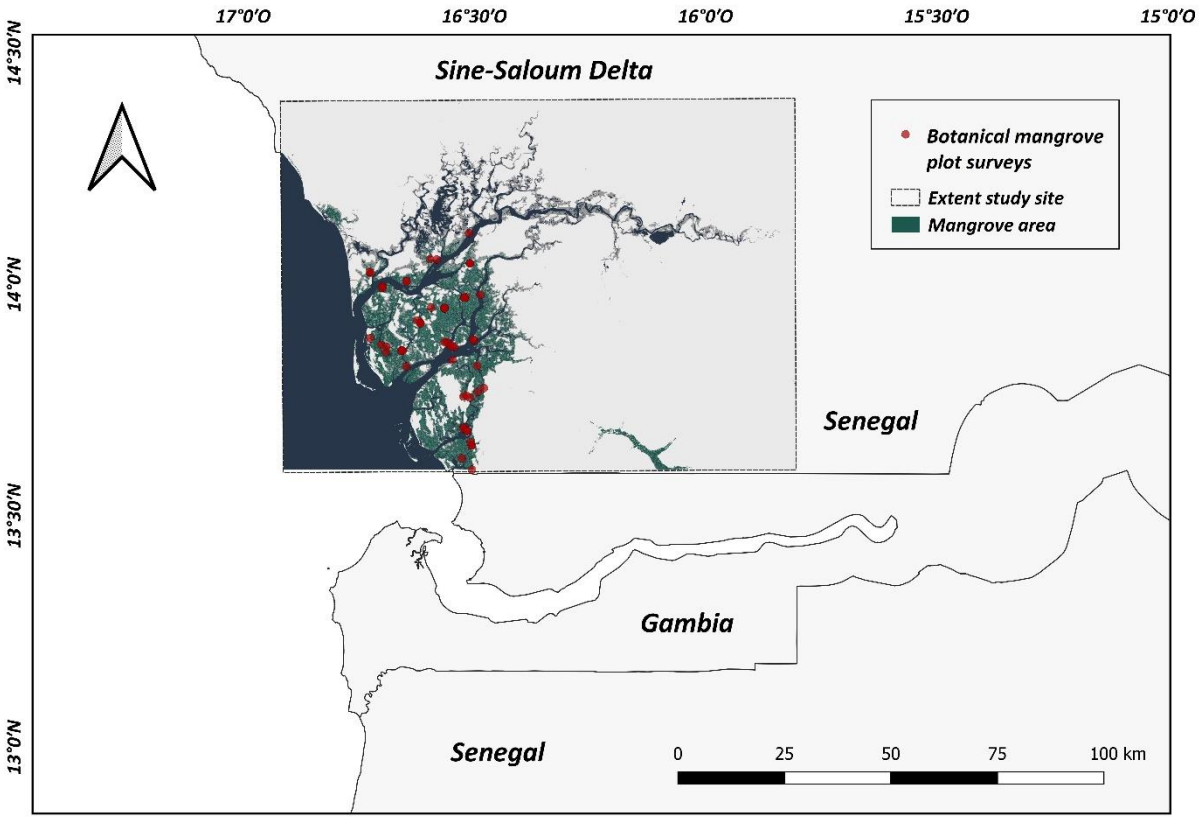

Figure 1: Extent study site and field-based inventory for mangrove zonation.

Sixty botanical surveys were performed and detailed the species, the extent of their relative abundance, and the height of the vegetation community.

2.2.Data collection and pre-processing

Sentinel-1 and Sentinel-2 images were selected for this study (Table 1). These data have been proven to be effective for mangrove mapping (Wang et al., 2018; Mondal et al., 2019; Wang et al., 2019; Jia et al., 2021; Lu and Wang, 2021; Lui et al., 2021; Xiao et al., 2021). The Sentinel-2 Level-2A data is available through Google Earth Engine. This product offers orthorectified Bottom-Of-Atmosphere (BOA) reflectances for all 12 bands in a 16-bit unsigned integer format that has been scaled by a factor of 10,000. We selected all available images (n = 79) from both sensors between 01/05/2020 and 01/06/2021 on the GEE platform. For Sentinel-2, the images were filtered with a value of 20% cloud cover. All processing of the S2 time series was performed on the unmasked pixels using 'QA60' quality layers. The range of the number of clear observations is from 47 to 65 cloud-free dates (Table 2). All spectral bands at 10 m and 20 m resolution of the Sentinel-2 sensor were retained. Bands at 20m were resampled at 10m. B1 and B9 were not included because they depict atmospheric traits, like aerosols, water vapor, and cirrus clouds, rather than reflecting surface characteristics of land-based features. The annual median was calculated for the optical spectral bands.

Table 1: Characteristics of Sentinel-1 and Sentinel-2 data

Sensor	Processing Levels	Acquisition Period	Relative orbit	Tiles
Sentinel 1	Level - GRD	01/05/2020 - 01/06/2021 (33 scenes)	133	-
Sentinel 2	Level – 2A	01/05/2020 - 01/06/2021 (79 scenes)	-	T28PBA, T28PCA, T28 PCAB, T28PBB, T28PDA, T28PDB

Table : The dates of observation for Sentinel-2 pixels that cloud-free are presented. These dates may differ for each pixel, and the dates shown depict those pixels with the minimum and maximum number of cloud-free days within the analyzed region

Year	Month	Days (65 cloud-free dates)	Days 47 cloud-free dates
2020	May	02, 07, 12, 17, 22, 27	02, 12, 17, 22, 27
	June	11, 16, 21, 26	11, 16, 21, 26
	July	01, 06, 21, 26, 31	01, 21
	August	05, 15, 20, 25, 30	15, 25
	September	09, 19, 24, 29	19, 24, 29
	October	04, 09, 14, 19, 24, 29	09, 14, 19, 24, 29
	November	08, 13, 18, 23, 28	08, 13, 18, 28
	December	03, 08, 13, 28	03, 08, 13, 28
2021	January	02, 07, 12, 27	02, 07, 27
	February	01, 06, 11, 16, 21, 26	21, 26
	March	08, 13, 18, 23, 28	03, 08, 13, 18, 28

April	02, 07, 12, 17, 22, 27	02, 07, 12, 17
May	02, 07, 12, 22, 27	07, 12, 22, 27

Four spectral indices were calculated. The normalized differential vegetation index (NDVI; Rouse et al., 1974) measures the active photosynthesis of vegetation using reflectance differences in the red and near-infrared wavelengths; it can be used to distinguish vegetation from other types of land cover. The near infrared surface water index (NDWI, McFeeters, 1996) measures the amount of water present on the surface of soils using reflectance differences in the near-infrared and mid-infrared wavelengths; it can be used to detect flooded areas and to distinguish mangroves from drier vegetation types (Gupta et al, 2018). The normalized difference moisture index (NDMI, Gao 1996), in particular the DBSI (Dry and Wet Soil Index) was designed to specifically identify bare areas in dry climates, according to Rasul et al. (2018). They were selected to identify the wet and dry areas constituting the sometimes semi-arid landscapes of the study area. The previously mentioned indices (NDVI, NDMI, NDWI, and DBSI) were used to calculate the GLCM textural indices introduced by Haralick et al. in 1973. Finally, time-series variables were used to complement reflectance and spectral indexes dataset. The phase and amplitude of the harmonic model (Clinton, 2016) were extracted from the annual time series of four spectral indices in the GEE.

The Sentinel-1 satellite imagery in the Earth Engine 'COPERNICUS/S1_GRD' image collection consists of Level-1 Ground Range Detected (GRD) scenes that have been processed to calculate the backscatter coefficient (σ°) in decibels (dB). The backscatter coefficient is a measure of how much microwave radiation is scattered back to the radar sensor by the target area and is expressed as the target backscattering area (radar cross-section) per unit of ground area. Since it can vary significantly, it is converted to dB by $10*\log10\sigma^\circ$. The backscatter coefficient can be used to determine physical characteristics of the terrain, including the geometry and electromagnetic properties of the terrain elements.

To calculate the backscatter coefficient, Earth Engine uses a series of preprocessing steps implemented with the Sentinel-1 Toolbox. These steps include applying orbit files to update metadata, removing low intensity noise and invalid data on the edges of the scenes, removing thermal noise in certain acquisition modes, applying radiometric calibration values, and correcting the terrain data using either the SRTM 30 meter or ASTER DEM. The terrain correction step converts the data from ground range geometry, which does not take terrain into account, to σ°, resulting in a more accurate representation of the terrain.

In the absence of top-down data for this area, only bottom-up data were selected, and the two polarizations (VH and VV) were combined. A total of 33 images for the period from May 1st, 2020 to June 1st, 2021 have been processed. For the SAR data, the ratio of VH to VV polarization (VH/VV) was calculated. Four variables were extracted from the VH, VV, and VH/VV bands over an annual time series: the median, minimum, maximum, and coefficient of variation (standard deviation divided by the mean). The dataset consisted of 102 predictor variables before being optimized through selection. (Table 3).

Table 3: A list of initial variables for classification level-1 (mangrove and land cover)

Sensor	Description	Bands name	Wavelength range	Resolution

Sentinel-2				
	Spectral bands			
		Band2 : Blue	458–523 nm	10 m
		Band3 : Green	543–578 nm	10 m
		Band4 : Red	650 – 680 nm	10 m
		Band5 : Red Edge 1	698–713 nm	20 m
		Band6 : Red Edge 2	733–748 nm	20 m
		Band7 : Red Edge 3	773–793 nm	20 m
		Band8 : NIR	785–900 nm	10 m
		Band8A : Red Edge 4	855–875 nm	20 m
		Band11 : SWIR 1	1565–1655 nm	20 m
		Band12 : SWIR 2	2100–2280 nm	20 m
	Spectral index		Formula	Reference
		NDVI	(B8-B4)/ (B8+B4)	Rouse et al. (1974)
		NDWI	(B3 – B8) / (B3 + B8)	McFeeters (1996)
		NDMI	(B8 - B11) / (B8 + B11)	Gao (1996)
		DBSI	B11 – B3)/(B11 + B3) − NDVI	
	Harmonic index *(calculated on the spectral indices)*			
		Phase	displacement between the origin and the peak of the wave in the range of 0 to 2π	Jakubauskas et al. (2002)
		Magnitude	half the value at which the function is maximized	Jakubauskas et al. (2002)
	Texture information *(calculated on the spectral indices)*			Haralick et al. (1973)
		Angular Second Moment: measures the number of repeated pairs		
		Contrast: measures the local contrast of an image		
		Correlation: measures the correlation between pairs of pixels		
		Variance: measures how spread out the distribution of gray-levels is		
		Inverse Difference Moment: measures the homogeneity		
		Sum Average		
		Sum Variance		
		Sum Entropy		

		Entropy: Measures the randomness of a gray-level distribution		
		Difference variance		
		Difference entropy		
		Information Measure of Corr. 1		
		Information Measure of Corr. 2		
		Dissimilarity		
		Inertia		
		Cluster Shade		
		Cluster prominence		
Sensor	Description	Bands name	Centre frequency	Resolution
Sentinel-1	SAR			
		VH- ascending	5.405 GHz	X: 10 m Y:10 m
		VV- ascending	5.405 GHz	X: 10 m Y:10 m
		VH/VV		
	SAR statistics on the time series *(calculated on VHasc, VVasc, VHasc/ VVasc)*			
		Minimum		
		Maximum		
		Median		
		coefficient of variation		

3. Methods

The complete methodological flowchart is shown in Figure 2. This method is divided into two levels:

Level 1: Mapping the mangroves and land use required for linear spectral unmixing

Level 2: Mapping vegetation formations by object-based spectral-temporal feature classification

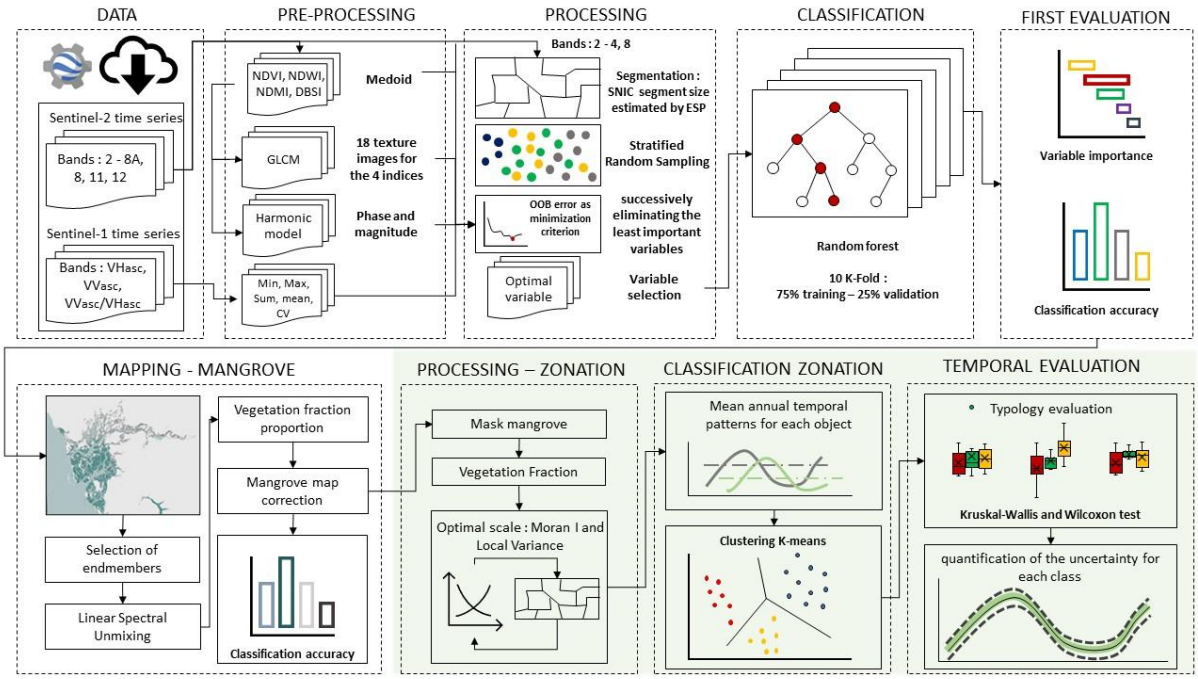

Figure 2: Flowchart of the proposed approach.

At white background: treatments allowing to obtain a cartography of the mangrove.

At light green background, treatments allowed us to obtain a cartography of mangrove plant formations.

3.1.Mangrove and land cover mapping (Level-1)

First, the mangrove is mapped using a combination of OBIA and machine learning approaches, specifically Random Forest. Although the pixel approach has been extensively used for mangrove classification (Bunting et al., 2018; Mondal et al., 2019; Jia et al., 2021; Lu and Wang, 2021; Lui et al., 2021; Xiao et al., 2021), we chose an object approach (Myint et al, 2008; Wang et al., 2018; Wang et al., 2021) to reduce spectral confusion by smoothing the dataset features within objects and reducing the statistical noise of the images (Blaschke et al., 2008; Blaschke, 2010; Dronova, 2015; Hossain and Chen, 2019). This reduces the complexity of the images and the size and dimensionality of the dataset. In addition, the optimal features for classification were evaluated. With textural characteristics, objects appear as a privileged entity to evaluate the importance of texture indices (GLCM) in classifying inter-tidal areas.

3.1.1. Segmentation

Segmentation is the first classification process. The superpixel clustering approach based on simple non-iterative clustering (SNIC) using the GEE was chosen. Bands with the highest optical spatial resolution only (B2, B3, B4, and B8) were implemented. The SNIC algorithm (Achanta and Süsstrunk, 2017) uses a regular grid of 'seeds' as the initial centroid of the superpixel. The parameterization of the algorithm requires the specification of superpixel seed spacing (in pixels). The larger the spacing, the larger the object size. Therefore, it is critical to scale parameters. Several methods have been developed to determine the optimal threshold for the scale parameters (Ma et al., 2017). The scale parameter estimation (ESP) initially proposed by Drăguţ et al. (2010) and modified for multispectral imagery (Drăguţ et al. 2014) was chosen because of its low computational cost, and therefore, could be applied to large areas. For each 2–50-pixel spacing step, the local variance was calculated for each band and then averaged

(Drăguţ et al. 2014) for fixed values of connectivity at 8 and compactness at 1. The rate of change (ROC) was then calculated for each scale change. The first break in the curve after continuous decay is the threshold at which significant objects emerge. In other words, the scale value showing for the first time a negative change (Figure 3) in the ROC curve was selected as the optimal seed spacing value.

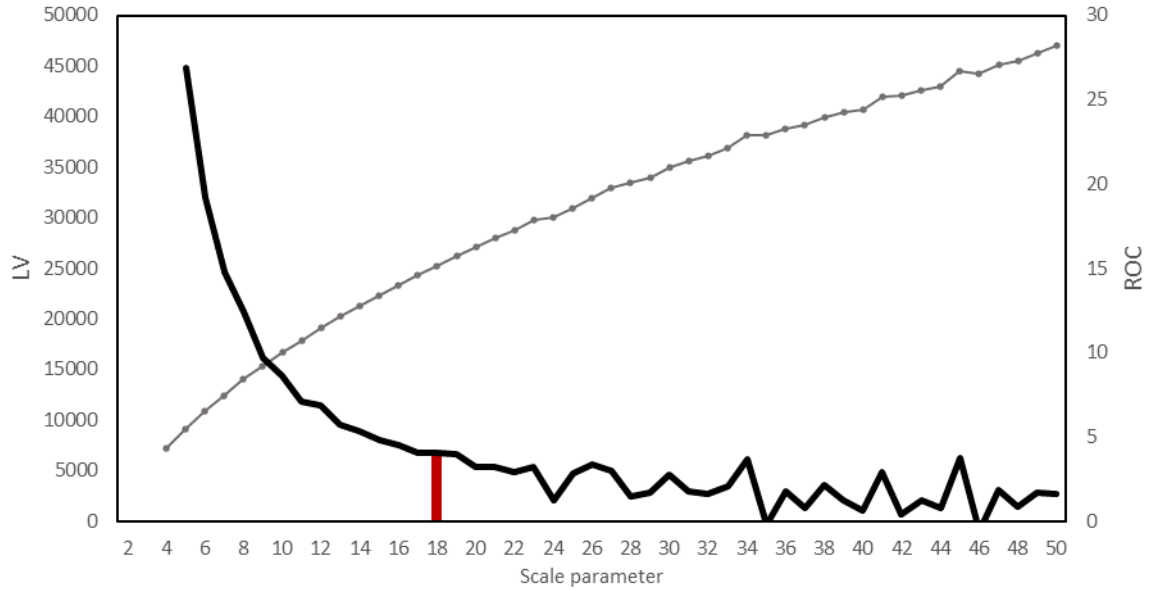

Figure 3: Estimate scale parameter.

The graphs show the changes in local variance (LV) (black) and rate of change (ROC) (gray dots) with increasing scale parameters. Vertical lines in red indicate the optimal scaling parameters selected for Saloum

3.1.2. Training and validation samples

The training and validation of machine learning classifications require reference sample data for land cover. Four classes were referenced: Water, Mangrove, Salt flats, Other land covers (all continental surfaces, including bare soil, other vegetation, urban, and cropland). Reference data collection followed a labeling procedure using ESRI (2017) and Google Earth (2018, 2021) high-resolution imagery, with a Sentinel-2 color composition check from 2021 to ensure the class stability spotted on slightly older THRS imagery.

Stratified random sampling was applied to avoid bias during the validation (Olofsson et al., 2014). Therefore, a random draw was performed in the nine classes of the ESA WorldCover 10 m 2020 v100 map (Zanaga et al., 2021) with 400 points per class. This map had an overall accuracy of 74.4%; therefore, we removed or corrected erroneous data. After filtering, 2592 reference samples were collected, of which 75% and 25% of the samples were retained for training and mapping validation, respectively. For model training, 223, 312, 322, and 1,660 samples were retained for water, mangrove, salt flats, other land covers, respectively. The objective was to obtain a statistical representation of the different land cover types within the dry land class. For model validation, 74, 77, 80, and 414 samples from water, mangrove, salt flats, other land covers, respectively, were selected.

3.1.3. Classification processing and accuracy assessment

The classification into water, mangrove, salt flats, other land covers was performed using the random forest algorithm (Breiman, 2001) on the GEE platform. Although the random forest model has the ability to handle many variables (Belgiu and Dragut, 2016), we chose to reduce the dimension of the dataset by retaining only the so-called optimal variables. To develop simple and parsimonious classification models, the use of a variable selection algorithm allows the maintenance of a small number of variables. This will allow for fewer data collection procedures in the future and a more efficient evaluation of the variable importance. Speiser et al. (2019) mentioned that reducing the number of variables in random forest models can also improve the efficiency of classification. To address these objectives, a backward elimination approach was used, based on model performance as a function of the rate of change in classification accuracy when adding or removing variables (Díaz-Uriarte and De Andres, 2006). The VarSelRF package in R statistical software was used to select variables. The 'Out of Bag' (OOB) error was used as a minimization criterion and the least important variables were eliminated. In each iteration, 10% of the variables were eliminated. This procedure was repeated 20 times, as recommended by Li et al. (2016) and Wang et al. (2018), to select a subset of the most important features. To assess the stability of the classifications, a 10-fold repeated cross validation was undertaken. The accuracy scores for mangrove, inter-tidal, and upland classifications were obtained using a confusion matrix (Stehman 1997). Overall accuracy (OA), producer accuracy (PA), user accuracy (UA), and kappa coefficients were generated. Finally, an overall F1 score was used to obtain the accuracies for each land cover class.

3.2.Mangrove zonation mapping (Level-2)

We also used the OIBA approach to map mangrove zonation by discriminating its plant formations. Segmentation is a crucial step and is performed using a linear spectral unmixing image of the vegetation fraction. The first mapping allowed for the selection of the endmembers. Based on the model of Taureau et al. (2019), we decomposed the pixel intensity into three endmembers, each representing a component of the mangrove ecosystem.: water, mangrove and salt flats. The 10th decile of the mangrove NDVI was retained. Mudflats with the lowest coefficient of variation of NDWI were chosen for their spectral stability throughout the year. Non-turbid water spectral was obtained by unsupervised classification of the water mask into 30 classes and selection of the spectral signature with the lowest reflectance values in the Sentinel-2 optical bands. The spectral signatures of the endmembers are shown in Figure 4.

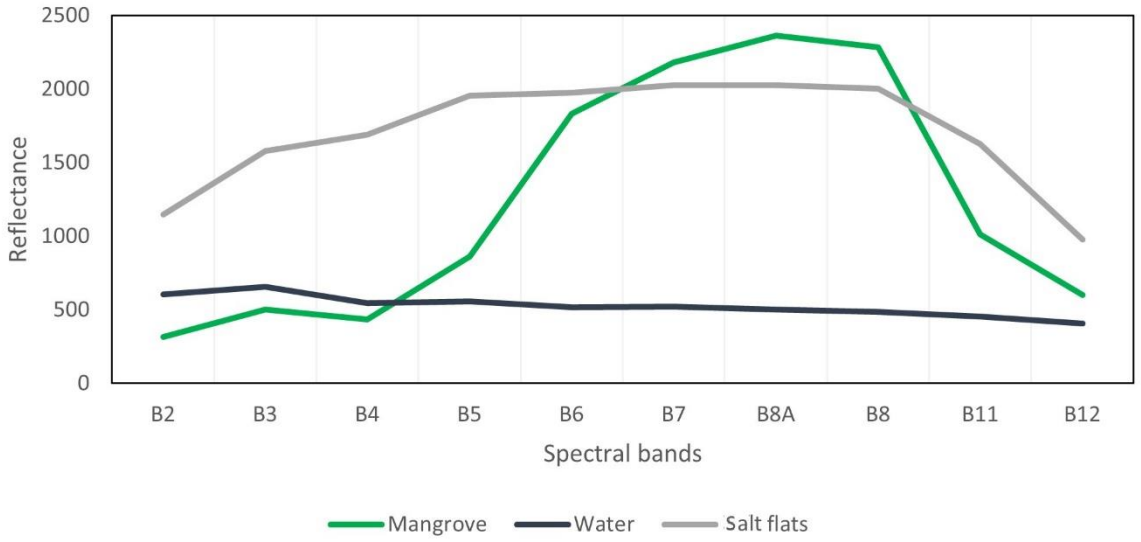

Figure 4: Spectral reflectance curves for water, mangrove, and salt flats selected for linear spectral unmixing.

Four images were generated to represent the contribution of each endmember to each pixel. Therefore, the pixels misclassified during the first step could be partially corrected by considering the most important contribution of the endmember to definitively assign the classes of mangrove, salt flats, and water. We preferred the OBIA approach in the first instance because the optimal object size avoids confusion between mangroves and dense dryland vegetation that was obtained using the pixel approach. Nevertheless, the optimal object size was calculated globally, not locally. Therefore, objects that are too large in areas of mangrove vegetation that combine water and salt flats may remain. Hence, Linear Spectral UnmixingLSU allows the pixels to be reassigned to the right classes within the objects.

3.2.1. Segmentation and spatial structure of the mangrove

Intra-mangrove segmentation is a key step in determining homogeneous features that reflect mangrove distribution along environmental gradients. The SNIC algorithm under GEE was used again by varying the superpixel seed spacing in steps of 1 and up to a spacing of 20. We considered that the 'optimal' intra-mangrove objects could not be larger than 20, because the optimal scale parameter for land cover classification was 18. The choice of the segmentation scale parameter is crucial because it will have important consequences on the clustering and thus the typology of vegetation formations. To better detect transitions within the mangrove, the selection of the optimal scale parameter must meet the criteria of intra-segment homogeneity and inter-segment heterogeneity (Espindola et al., 2006; Johnson and Xie, 2011; Johnson et al., 2015). For this purpose, the most common method is to calculate the weighted variance (wVar) as an indicator of intra-segment spectral homogeneity (Eq. 1) and the Moran Index (MI) to measure the inter-segment spectral heterogeneity (Eq. 2).

$$wVar = \frac{\sum_{i=1}^{n} a_i \times v_i}{\sum_{i=1}^{n} a_i} \qquad (1)$$

where n is the total number of objects

$v_i$and a_i are the variance and area of the object i, respectively. Large objects have a greater impact on the overall variance than small ones.

$$MI = \frac{n \sum_{i=1}^{n} \sum_{j=1}^{n} w_{ij}(y_i - \bar{y})(y_i - \bar{y})}{\sum_{i=1}^{n} (y_i - \bar{y})^2 (\sum_{i \neq j} \sum w_{ij})} \quad (2)$$

where n is the total number of objects

y_i and $\bar{y}$ are the average spectral values of the object i and the whole image

w_{ij} is a measure of the spatial proximity between object i and j.

For the calculation, the objects were in a vector format. We considered the adjacency of the segments as spatial proximity; if a single vertex of an entity is adjacent to another entity, these two segments are neighbors. Therefore, we constructed a matrix of spatial weights. Several studies (Johnson and Xie, 2011; Wang et al., 2021) have set the values of w_{ij} to zero (non-neighbor) or one (neighbor). Binary matrices can induce statistical bias, generating different weights for individuals depending on their neighbor numbers. To overcome this problem, in-line standardization of the matrix was performed. Thus, the sum of the weights in each row is equal to one. This operation was performed with the package 'spdep' in R (Bivand et al., 2015).

The values of wVar and MI were normalized for comparison according to the following normalization formula (eq. 3):

$$X_{norm} = \frac{(X - X_{min})}{(X_{max} - X_{min})} \quad (3)$$

Where X_{norm} is the normalization of the values of wVar or MI.

X_{min} is the minimum value of wVar or MI.

X_{max} is the maximum value of wVar or MI.

Finally, the F-measure was calculated (eq. 4) to capture the best compromise between intra-homogenous and inter-heterogenous segmentation (; Johnson et al., 2015; Wang et al., 2019).

$$F = \frac{1}{\alpha \frac{1}{wVar} + (1 - \alpha) \frac{1}{MI}} \quad (4)$$

where α (between 0 and 1) is the relative weight of the normalized values of wVar and MI. Thus, intra-segmental homogeneity or inter-segmental heterogeneity can be assigned higher importance. In this study, the weights of the two indices are considered the same. Therefore, the weight was set as α = 0.5. A large F-value indicates high-quality segmentation.

3.2.2. Clustering of mangrove zonation

To capture this cycle, the time series of the plant fraction was modelled using harmonic regression in GEE (Clinton, 2016). This method has been shown to be relatively effective in describing mangrove zonation patterns in semi-arid areas with Sentinel-2 images (Valderrama-

Landeros et al., 2021). Therefore, regression models with harmonics were used. We fitted and calculated the harmonic coefficients and extracted the amplitude (seasonal variability), annual trend (annual average), and RMSE (non-seasonal variability) to characterize the phenological patterns of the different objects (Pasquarella et al., 2018). Model fit was better for harmonic regressions based on fractional components from linear unmixing than for spectral indices, justifying the use of the vegetation fraction instead of NDVI. The objective here is to discriminate these zonations on an annual basis rather than revealing the variation itself. The annual average is indeed a feature that mostly influences classification.

The small sample size from the field made the training and validation process of a supervised classification difficult; therefore, unsupervised classification with the K-means algorithm was preferred. The objective was to obtain a typology aimed at maximizing the contrasts between classes while reflecting the zonation and physiognomy of the vegetation. Field data were used to interpret the clusters. To ensure the overall significance of the classes, the Kruskal-Wallis test was performed. In addition, pairwise multiple comparisons between groups were used to evaluate the significance between classes using the Wilcoxon test. These tests were performed with field-derived variables, such as cover rate, stand height, and species dominance. These tests were performed with all variables of the harmonic model describing seasonality and with different numbers of classes from two to six. To evaluate the significance of the differences between classes, the threshold p-value of 0.01 was retained.

3.2.3. Stability assessment of the typology

The detection of mangrove zonation typology must be reproducible over time to ensure its monitoring and reliably interpret its changes. Indeed, a typology in which the classes do not have enough contrast at certain times of the year could lead to errors in detecting changes.

To evaluate typology and temporal stability, we used a three-step process. First, the methodological chaining presented so far was repeated on the data from 01/11/2019 and 01/11/2020. An intersection between the two classifications allowed us to isolate the objects assigned to the same class on both dates, which did not undergo any major changes. Finally, these were used as a basis for training (70% of the objects) and validation (30% of the objects) of the Bayesian model. For this stage, the probabilities of membership were calculated using Bayes' theorem.

$$\mathrm{p}\,(\mathrm{h} \mid e) = \frac{p(e \mid h) \times p(h)}{\sum_i p(e \mid h_i) \times p(h_i)} \qquad (5)$$

where p(h | e) is the probability that hypothesis (h) is true, given the proof (a posteriori probability noted e).

p(e | h) is the probability of finding that the evidence provided by hypothesis (h) is true (from the training data).

p(h) is the probability that the hypothesis is true, regardless of the evidence (a priori probability).

A series of images expressing the *a posteriori* probability of belonging to a set of plant formation classes were generated. The objective of this study was to evaluate the degree of belonging of an object to a class according to the vegetation fraction on both dates. Hard

classification was used to obtain a thematic map. For each object, the class with the highest probability was assigned.

Finally, the probable confusion over time was evaluated for each class by noting the frequency of false predictions of the Bayesian model for each value of the vegetation fraction. The objective of this experiment was to quantify the amplitude of the fluctuations in plant fractions that can be interpreted as a change in the spatial structure of mangrove zonation.

4. Results

4.1.Mangrove mapping

At the end of the RF classification of the objects, the Saloum mangrove map (Figure 5a) presented relatively high accuracy scores (Table 4) using a reduced dataset of 11 discriminating variables. After ten cross-validations, the optical bands in the NIR and SWIR wavelengths proved to be the most effective for mapping the mangrove in this environment, followed by the SAR data (Figure 5b). From then on, the SAR data constituted more than 50% of the selected variables. Texture variables and time-series harmonic model coefficients were negligible for the desired land cover discrimination. Finally, 11 variables were selected: VHmin, VHmed, VHmax, VVmin, VVmed, VVmax for SAR data and B8, B8A, B11, B12, NDWI for optical data. The consistent appearance of SAR data in the group of optimal variables suggests that it is a valuable source of information for understanding and predicting the distribution and behavior of the studied system. In contrast, when optical bands like B8 or B8A were present in the group of variables, they tended to contribute more to the discrimination of the surface states of the selected typology.

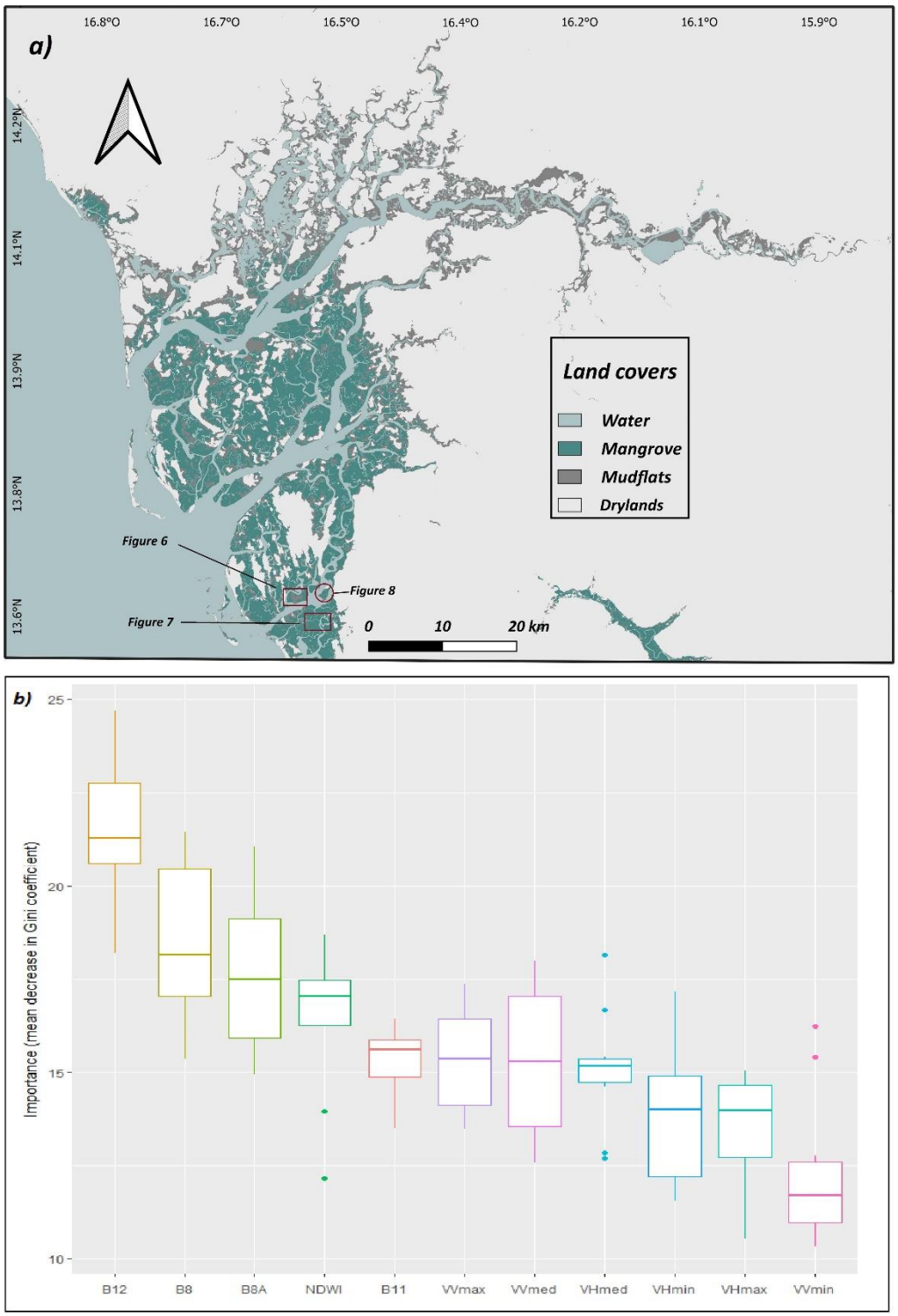

499

500 **Figure 5a**: Random Forest classifications using Sentinel-1 and Sentinel-2 data (left) from an optimal dataset.

501 Locations refer to the following figures that focus on mangrove zonation

502 **Figure 5b**: Optimal dataset and variables importance.

503 The importance of the variables was measured by the average decrease in the Gini index of the nodes and leaves
504 in the resulting random forest. This expresses the degree of precision that the model loses by excluding each
505 variable.

506

Table 4 shows that the average overall accuracy is 97.12% and the Kappa index is 94.6%. Within the Sine-Saloum region, mangroves obtain the highest average relative accuracy scores (F1-score = 98.55%) among the land cover types. Drylands has similar scores, and salt flats had the lowest average accuracy with an F1-score of 88.31. On the other hand, the classifications are relatively stable. Indeed, the standard deviation for the global accuracies and Kappa index are 0.008 and 0.015, respectively. The surfaces and their fluctuations were quantified according to the classifications. The water and mangrove areas varied respectively by an average of 0.37% and 0.47%, that is, 721 ha and 317 ha. Variations of 0.1%, that is 756 ha, were observed on average for the drylands. Finally, the salt flats showed more important fluctuations in the estimation of their surfaces, of the order of 2% or 1029 ha.

Table 4 shows that the contribution of post-classification linear spectral unmixing brings a slight gain in overall precision (+ 0.99%) and (+ 1.88%) on the Kappa index. We also observed a significant gain in relative precision class by class. Nevertheless, the LSU contribution is sometimes better at the pixel level than at the object level, notably for water (F1 score = + 1.95 against 1.39 for RF-OBIA + LSU-OBIA) and mangroves (F1 score = + 0.36% against -1.33 for RF-OBIA + LSU-OBIA). Given the scores and the purpose of this paper, the mangrove areas from the RF-OBIA + LSU method were retained for mapping the vegetation formations.

Table 4: Scores assessing the accuracy of the classifications and their impact on the quantification of Land Cover types

Accuracy	*OA %*		*Kappa %*		*F1 - Score %*			
	Mean	*Std*	*Mean*	*Std*	*Water*	*Mangrove*	*Salt flats*	*Drylands*
(*RF-OBIA*)	97.12	0.8	94.6	1.5	96.30	98.55	88.31	98.53
(RF-OBIA + LSU-OBIA)	98.11	0.8	96.48	1.5	97.69	97.22	92.16	99.46
(*RF-OBIA + LSU*)	97.55	0.9	95.42	1.7	98.25	98.91	90.10	99.35
Area	*Area (ha)*				*Std Area (ha)*			
	Water	*Mangrove*	*Salt flats*	*Drylands*	*Water*	*Mangrove*	*Salt flats*	*Drylands*
(*RF-OBIA*)	193 214	67 762	50 380	750 382	721	317	1 029	756
(RF-OBIA + LSU-OBIA)	192 843	65 341	53 188	749 373	-	-	-	-
(RF-OBIA + LSU)	193 578	63 124	54 762	750 272	-	-	-	-

The linear spectral unmixing measuring, within a pixel, the fraction of each land cover showed that the initial (object-based random forest) classification overestimated the mangrove areas by an average of 4638 ha or 6.84%. The consequent decrease in mangrove surfaces with the RF-OBIA + LSU approach coincided with the increase in salt flats surfaces. Therefore, the main confusion concerns the mangroves and salt flats. Of the mangrove surfaces, 6.43% were

classified as salt flats using the RF-OBIA + LSU approach, and 0.42% as water. Therefore, 93.5% of the classification differences between the two approaches concerned mangroves and saltflats (Figure 6).

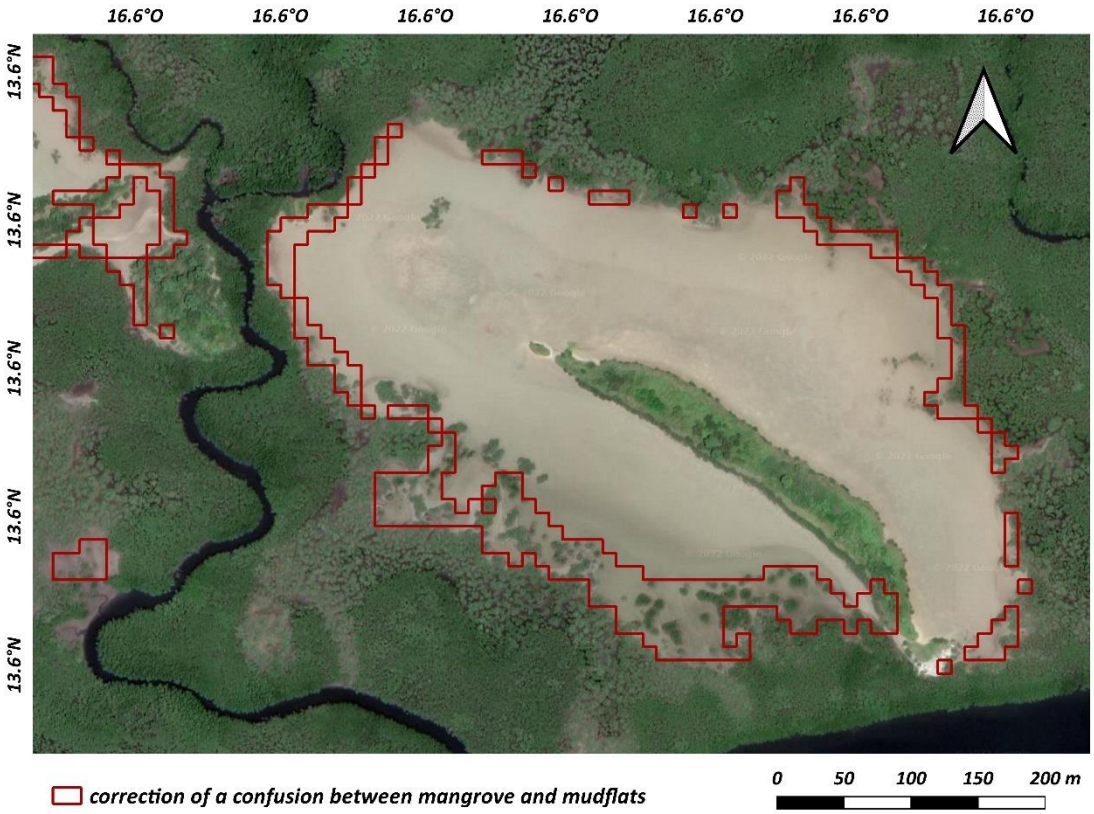

Figure 6: Example of correction of the RF-OBIA +LSU approach. Red contours represent areas classified as mangrove before correction and as salt flats after correction. Most of the confusion concerns the mangrove-salt flats interface.

4.2. Mangrove zonation mapping

4.2.1. Optimal scale

Figure 7 shows the optimal scale obtained by maximizing inter-segment heterogeneity and intra-segment homogeneity. A spacing of nine pixels allows the SNIC approach to achieve an optimal global trade-off. The spacing from 2 to 11 pixels generated objects with a very different internal variance from one spacing to the other, increasing faster before the slope of the curve became smoother. The Moran index decreased consistently over the same interval, meaning that the objects diverge increasingly from their neighborhood. The F-metric allows the best global compromise to be synthesized. Therefore, the tested spacings from 2 to 8 induced a satisfactory internal homogeneity of the objects, but an extremely low global inter-object heterogeneity. A spacing of 2–8 induced over-segmentation; thus, the tested spacings from 10

to 20 induced extremely low intra-object homogeneity, but acceptable global inter-object heterogeneity. Therefore, we concluded that a spacing of 10–20 induces under-segmentation.

Figure 7 shows the consequences of the chosen scale on vegetation fraction index segmentation (Figures 7b and 7c). A THRS Google Earth image (Figure 7a) allows for apprehending the grain of the vegetation, its retranscription by the vegetation fraction index (Figure 7b), and the consideration of its spatial structure by segmentation (Figure 7c). Visually, the strong values of the index (in red) synonymous with a high and dense mangrove, often at the edge of banks, seem well-captured as a single object by the OBIA approach. On the other hand, some places where the index is lower and where the vegetation cover appears less dense on the THRS image appear oversegmented.

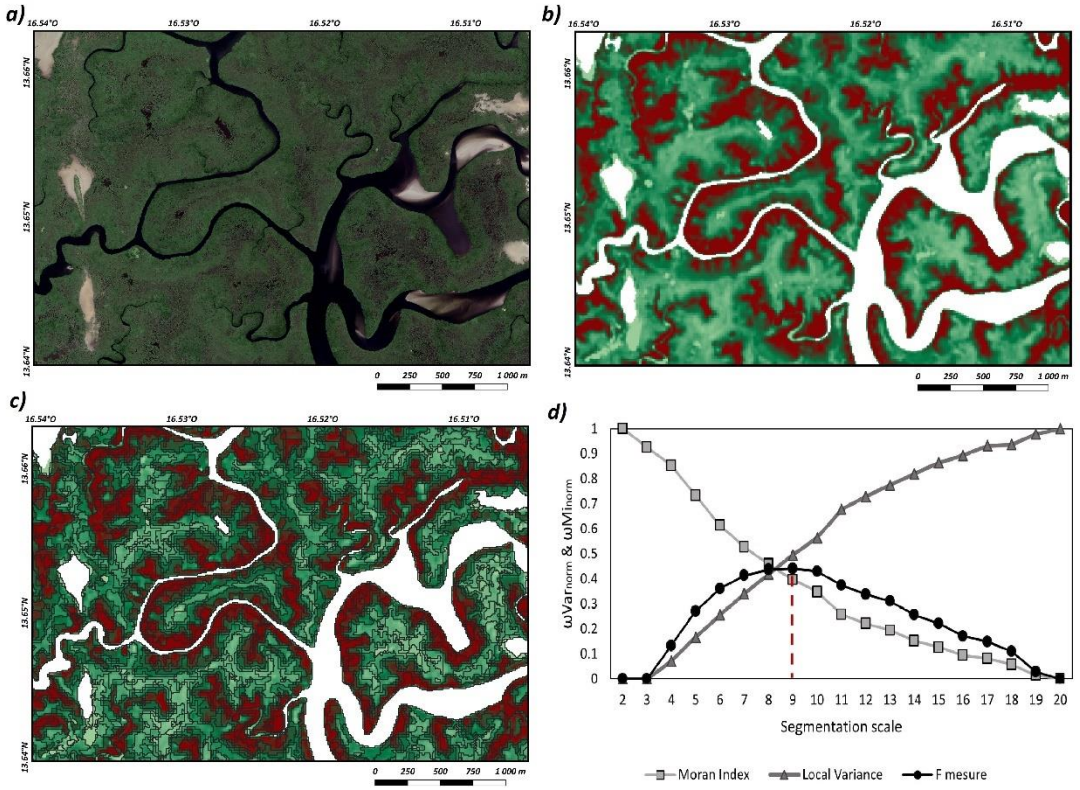

Figure 7: Optimal segmentation scale for detecting homogeneous plant formations.

a) High resolution Google Earth image of South Saloum

b) The vegetation fraction index from linear unmixing (Red values represent the largest vegetation fraction and can be equated with dense, high shoreline mangroves. The green gradient can be assimilated into the decrease in the density and height of the mangrove along the foreshore)

c) Optimal object segmentation

d) Results of optimal scale parameter detection. The 9 pixels spacing for SNIC segmentation is the best compromise between intra-homogenous and inter-heterogeneous segmentation.

4.2.2. Spectral Seasonality-Based Mangrove Zonation Classification Using Spatial Objects

581 The vegetation indices of these mangroves followed a seasonal pattern that could be captured
582 by the vegetation fraction of a pixel. High values of the vegetation fraction index were
583 observed during the rainy season, mainly from August onwards. A decrease in these values
584 was observed at the end of the rainy season in November.

585 The discrimination of mangrove plant formations by time-series analysis meets the objective
586 of developing a reliable and robust typology over time. Figure 8 shows that during the course
587 of the year, the values of the indices do not always capture contrasts in the spatial structure of
588 the vegetation. Indeed, at the end of the dry season, there were sometimes no differences in
589 plant fraction index values between the two plant formations. The values obtained for
590 18/06/2020 and 02/04/2021 (fig. 8) were similar between the high bank mangrove (HM) and
591 the low and dense mangrove (LDM), and between the latter and the low and open mangrove
592 (LOM). Therefore, single-date images and classifications based on the values alone may be
593 inoperable.

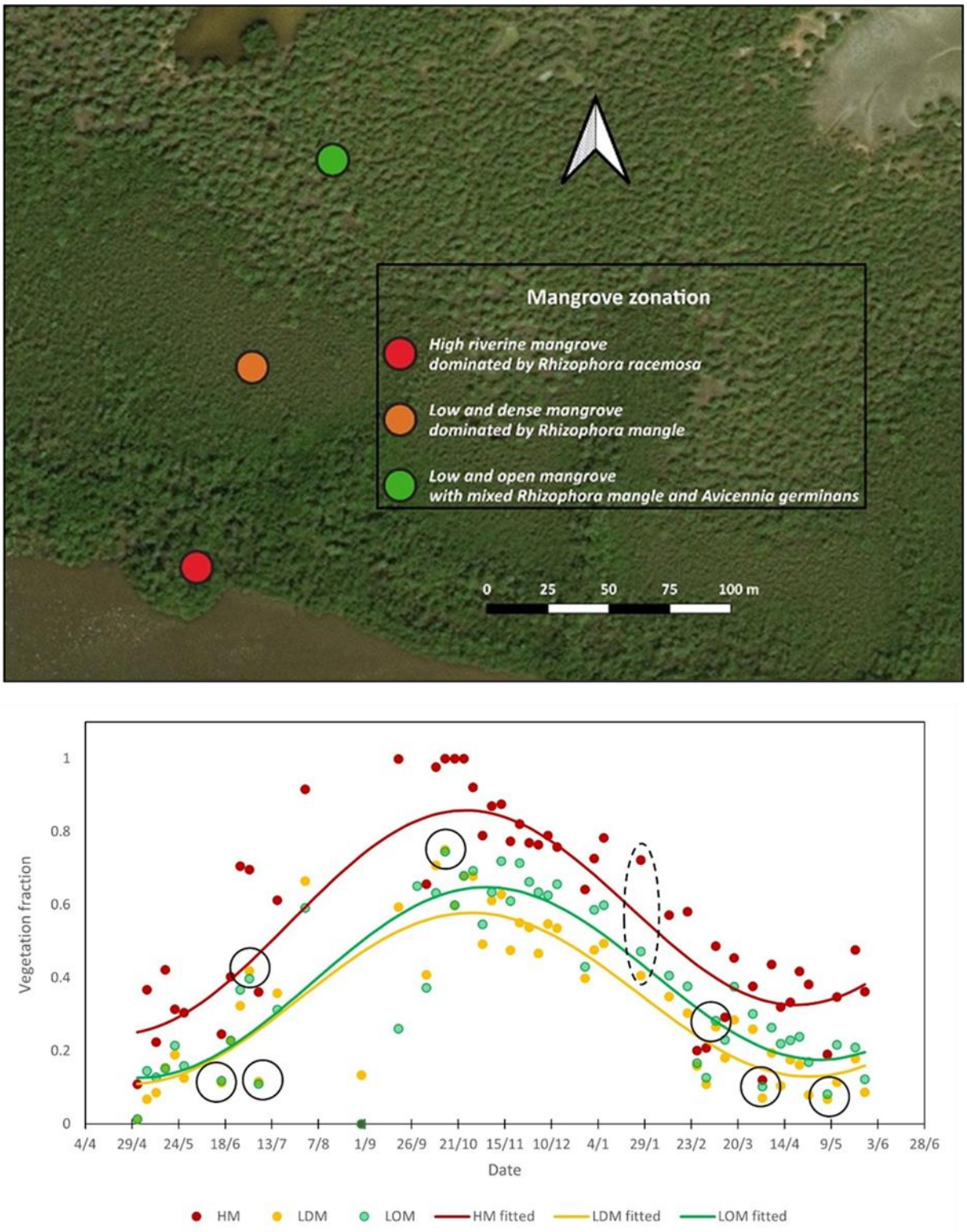

Figure 8: Annual phenological patterns of mangrove zonation.

On the x-axis, the time axis ranges from 2020-05-01 to 2021-06-01. On the y-axis, the vegetation fraction values from the linear spectral unmixing are shown.

The points represent the values within the time series for each class.

The solid lines represent the harmonic regression model for each class.

Solid line ellipses show the likely confusion between thematically different classes. The dashed ellipse represents the date when spectral sparsity is maximized.

HM : High mangrove – LDM : Low and dense mangrove - LOM : Low and open mangrove

Figure 9 shows the mangrove zonation clustering for 2021 and a visual comparison with Google Earth © images. The number of classes was determined from field data. The Kruskal-Wallis test was used to ensure the overall significance of the classes. The Wilcoxon test was used to determine whether the typology presented significant differences between classes with the parameters found in the field. The results of the different tests show that clustering based only on the annual average of the values modelled by harmonic regression and with three classes made the most thematic sense. These results indicate that the density of vegetation cover contributes significantly (p-value = 0.00057) to the discrimination of facies using the proposed approach. The three-class typology based on canopy height, canopy openness, and color appeared to fit well with the spatial resolution of the Sentinel-2 images (Figure 9). The differences in height between the second and third classes were not statistically significant (p-value = 0.102). Therefore, these two classes were denoted as low mangroves. Nevertheless, the proposed approach does not allow for the differentiation of mangroves at a specific level. It also does not allow for a significant determination of the abundance of species within the classes (Supplemental material). Therefore, a typology based on height, density of vegetation cover, and the presence/absence of plant species was adopted (Figure 9, Supplemental material). Finally, the morphology of the classes and their locations (Figure 9) seem to agree with the high-resolution data and with theoretical and empirical knowledge of the field (Sow et al., 1991; Ndour et al., 2012; Andrieu et al., 2020).

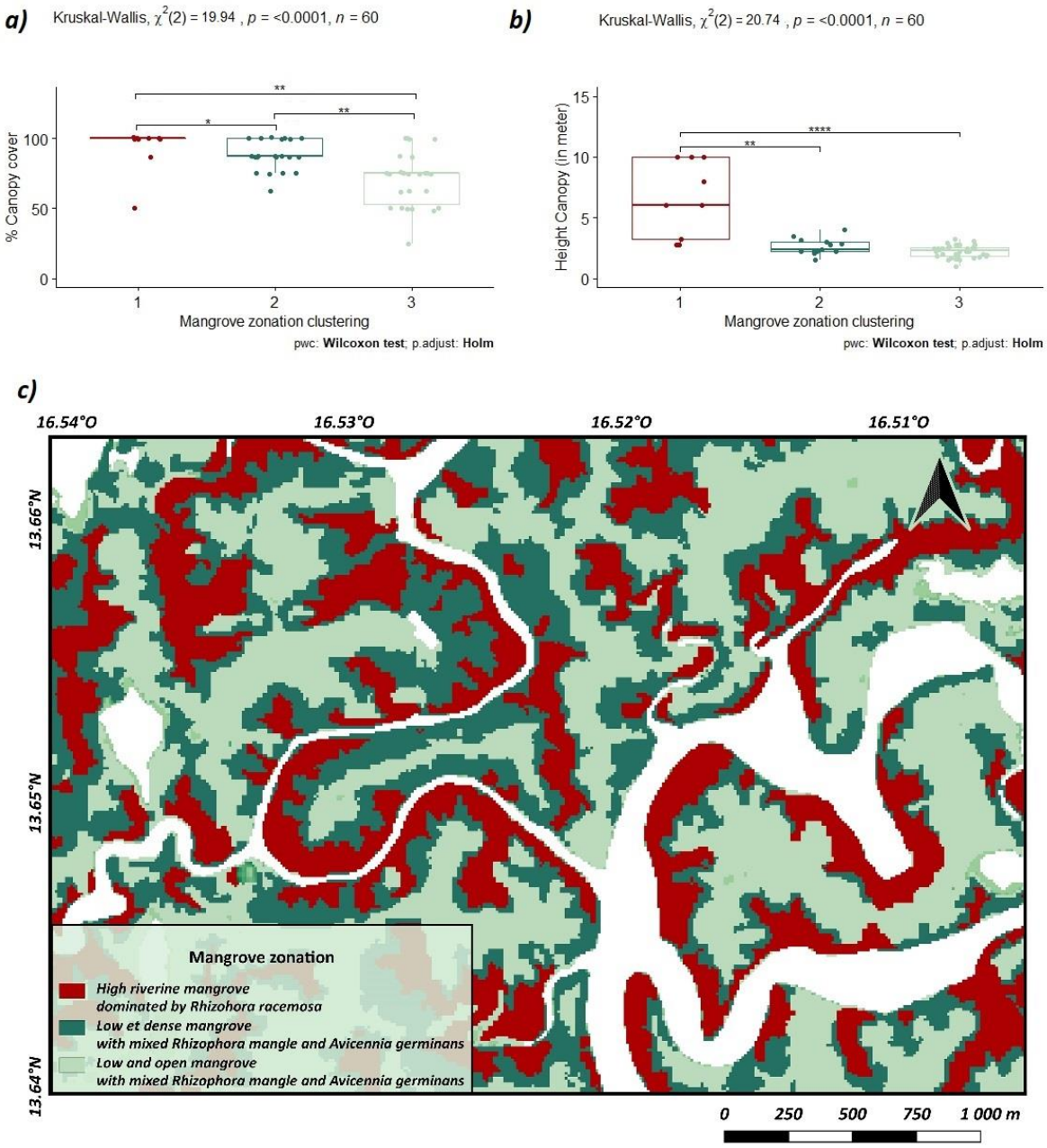

Figure 9: Mangrove zonation clustering

(1: High riverine mangrove dominated by *Rhizophora racemosa*; 2: Low et dense mangrove with mixed *Rhizophora mangle* and *Avicennia germinans*; 3: Low and open mangrove with mixed *Rhizophora mangle* and *Avicennia germinans*)

a) Significance of the differences between classes for the overlap rate.

(The results of the Kruskal-Wallis test are available at the top of the figures)

b) Significance of the differences between classes for the average height of the individuals

(Only the results of the significance tests appear in this figure).

c) Map of the mangrove zonation for the year 2021

The high mangrove facies have patches with rather long morphologies and are located at the edge of the channel. Patches of this class located in the middle of a mangrove area may indicate the presence of a small channel that is completely covered by a closed canopy. The low and

open mangrove facies showed a less elongated morphology and were consistently found at the interface with the salt flats. Finally, the low and dense mangrove facies were generally located between the other two classes, representing the transition between high-density and open mangroves. The ground-truth data also confirmed that not all riverine mangrove facies were necessarily high. In most concave meanders of channel banks, mangrove forests were medium and dominated by the *Rhizophora mangle*. Conversely, in most convex meanders of banks, mangrove forests were abundant and dominated by *Rhizophora racemosa*.

4.3.Temporal accuracy

Figure 10 shows the confounding probabilities for each class as a function of the plant fraction values. These reflect the average values obtained by harmonic regression between 2019 and 2021. The overall expected accuracy for classifying the mangrove plant formations in the Saloum Delta was 85.5% (Table 5). Confusion probabilities were the highest in classes that often have spatial contiguity in zonation. Consequently, the class 'Low and dense mangrove with mixed *Rhizophora mangle* and *Avicennia germinans*' had the highest prediction error rate. This class is likely to be confused with the 'High riverine mangrove dominated by *Rhizophora racemosa*' class with a probability of 5.8%, and with the 'Low and open mangrove with mixed *Rhizophora mangle* and *Avicennia germinans*' class with a probabbility of 8.3%. Table 5 presents the confusion matrix from the Bayesian classification. Logically, the prediction errors between the two classes located at the lowest and highest positions of the foreshore were negligible.

Table 5: The error matrix for the period (2019-2021) using a Naïve Bayes classification approach on stable objects (results are expressed as a proportion).

	Reference data		
Class	High riverine mangrove dominated by *Rhizophora racemosa*	Low and dense mangrove with mixed *Rhizophora mangle* and *Avicennia germinans*	Low and open mangrove with mixed *Rhizophora mangle* and *Avicennia germinans*
High riverine mangrove dominated by *Rhizophora racemose*	*26.3 %*	*3 %*	*0.2 %*
Low and dense mangrove with mixed *Rhizophora mangle* and *Avicennia germinans*	*2.8 %*	*28.5 %*	*4.6 %*
Low and open mangrove with mixed *Rhizophora mangle* and *Avicennia germinans*	*0.1%*	*3.7 %*	*30.7 %*
Overall accuracy (%)	*85.5 %*		

To evaluate the probability of confusion between real change in vegetation cover and seasonal fluctuation observed by remote sensing, uncertainty bounds were calculated for each class of zonation. Figure 10 shows the probability of confusion between classes as a function of the vegetation fraction from linear spectral unmixing. The cumulative frequency curve quantifies the proportion of the class subject to probable errors as a function of the plant fraction value.

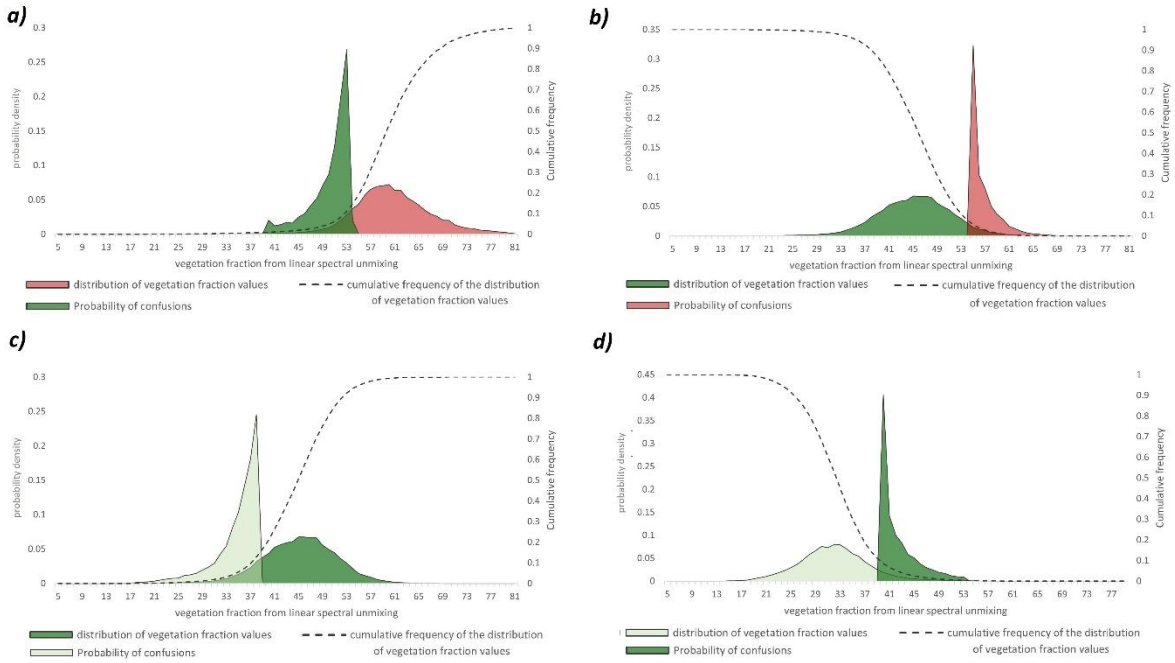

Figure 10: Probability of confusion between classes according to the values of plant fraction from the linear spectral unmixing.

Red represents 'High riverine mangrove dominated by *Rhizophora racemosa*'

Dark green represents 'Low and dense mangrove with mixed *Rhizophora mangle* and *Avicennia germinans'*

Light green represents 'Low and open mangrove with mixed *Rhizophora mangle* and *Avicennia germinans*'

Probable confusion between «High riverine mangrove dominated by *Rhizophora racemosa*» and «Low and dense mangrove with mixed *Rhizophora mangle* and Avicennia germinans»

a) Probable confusion between "Low and dense mangroves with mixed *Rhizophora mangle* and *Avicennia germinans*" et "High riverine mangrove dominated by *Rhizophora racemosa*".

b) Probable confusion between "Low and dense mangrove with mixed *Rhizophora mangle* and *Avicennia germinans*" et "Low and open mangrove with mixed *Rhizophora mangle* and *Avicennia germinans*".

c) Probable confusion between "Low and open mangrove with mixed *Rhizophora mangle* and *Avicennia germinans*" et "Low and dense mangrove with mixed *Rhizophora mangle* and Avicennia germinans"

Plant fraction values ranging from 61% to 100% were reliable for assigning to the class 'High riverine mangrove dominated by *Rhizophora racemosa*'. Next, the class 'Low and dense mangrove with mixed *Rhizophora mangle* and *Avicennia germinans*' had a plant fraction range between 38% and 52%, which does not seem to suffer from uncertainties. Finally, values below 33% seem to be reliably assigned to the class 'Low and open mangrove with mixed *Rhizophora mangle* and *Avicennia germinans*'. For clarity, Table 6 summarizes the uncertainty bounds of the classes.

Table 6: Uncertainty intervals for assigning classes over time according to the plant fraction values. The vegetation fraction is expressed here as a percentage.

	Class		
	High riverine mangrove dominated by *Rhizophora racemosa*	Low and dense mangrove with mixed *Rhizophora mangle* and *Avicennia germinans*	Low and open mangrove with mixed *Rhizophora mangle* and *Avicennia germinans*
1st Quartile	58	42	29
Median	61	46	33
3rd Quartile	65	50	36
Incertitude	*52 % < VF < 61 %*	*38 % > VF > 51 %*	*33 % < VF < 38 %*

According to these results, the densification of the low mangroves can be reliably interpreted only if the class values cross the threshold of a vegetation fraction higher than 38% (or more). Conversely, the opening of the low mangrove can be reliably interpreted at a threshold of 33% (and below) vegetation fraction. A disturbance in the high shoreline mangrove can be credibly detected only if the values of this class fall below the threshold plant fraction of 52%. Conversely, a recovery can be reliably detected if the values of the low dense mangroves cross the 61% vegetation fraction threshold.

5. Discussion

5.1.Extraction of significant objects for mangrove monitoring

The databases on mangroves in West Africa cover only the surface area. Zonation maps are desirable for guiding conservation strategies (Jia et al., 2018; Wang et al., 2019). However, global or continental databases contain inaccuracies that bias the mapping of plant formations. Here, the differentiation of the mangroves approaches an accuracy of 98.91%, in line with those obtained by Andrieu et al., 2020 and Liu et al., 2021. We aimed to establish a map of mangroves because the quantifications of surfaces in the literature have significant discrepancies.

Fent et al. (2019) reported areas of 86 426 ha in 2018 for the same spatial coverage of 30 m. Liu et al. (2021) made their data freely available. For the same spatial extent, in 2017, the extent of areas reached 70 140 ha at 20 m. Andrieu et al. (2020) mentioned a surface area of 63 189 ha at 30 m, in 2015, for the mangrove of the Saloum and Joal hydrosystems, but without the mangrove of the Gambia River tributary, which is within the administrative boundaries of Senegal. In this study, we obtained a surface area of 60 988 ha in 2021 at a spatial resolution of 10 m. A cartographic comparison showed that the areas mapped by Liu et al. (2021) were overestimated (Supplementary material). The mapping had inconsistencies; for example, some water channels were mapped as mangroves. However, this mapping was carried out over the entire West Africa, and currently, it is the most accurate database for all West African mangroves at this scale. Furthermore, the areas were likely overestimated by Fent et al. (2019) because the values were widely higher than those estimated by other studies (Andrieu et al., 2020; Liu et al., 2021).

Plant formations were mapped on a mangrove mask using the OBIA approach. The vegetation fraction was segmented by linear spectral unmixing. The OBIA approach is preferable for many reasons. First, the vegetation facies of Senegalese mangroves comprise one or more species. Owing to the global biogeography of mangroves (species rich in Southeast Asia but poor in Africa) and the occasionally arid climate, Senegalese mangroves show poor species richness, and are often monospecific in patches larger than a 10m pixel. Li et al. (2019) achieved overall accuracy scores of 83% for species mapping in China. Nevertheless, the species differentiated in this study have their own phenological patterns, which is not the case in the Saloum Delta. Indeed, even in monospecific pixels or objects, spectral contrasts in the time series appear essentially in the average annual trend and phenological patterns. Valderrama-Landeros et al. (2018) achieved scores ranging from 75% to 78% at a specific level and 10 m resolution. Vizcaya-Martínez et al. (2022) achieved accuracy scores between 92 and 95% for the classification of species with VIs from S2 images. Using the time series, the authors were able to follow the recovery trajectories of mangrove zoning after disturbance, similar to the zoning presented in this work in Senegal. However, in our case, the upper mangrove was mixed within a pixel, and we did not claim to classify the species. Therefore, working on a plant formation scale is preferable. Transitions between plant formations are noticeable through changes in the relative density of the genera *Rhizophora* and *Avicennia*, and changes in vegetation physiognomy. Therefore, our typology converges with that of Valderrama-Landeros et al. (2021). These authors obtained an overall accuracy of 79% for similar mangroves, both on their specific content and on canopy density variations. Through remote sensing, these transitions are identifiable, and these plant formations are detectable using object-oriented approaches, as demonstrated by Flores De Santiago et al. (2013) and Wang et al. (2018). Plant formations are relevant units for detailed assessment of the impacts of environmental changes on mangroves. Monitoring the fluctuation of zonation over time is challenging, and a typology based on an object-oriented approach would allow for monitoring of plant formations with similar ecological properties. A pixel-based approach could lead to a heterogeneous cartographic result without an ecological context and, therefore, is not interpretable. Moreover, the zoning of the mangrove was unsupervised. Field observations have shown that the species abundance may be heterogenous within an entity equivalent to a pixel. In addition, in most pixels and surveys, one of the three species that were abundant in Saloum was absent. This generates zero inflation, which requires the use of other statistical methods to obtain the relevant pixel-scale information. The OBIA approach circumvents this problem and allows us to work on a scale where a specific mixture constitutes detectable and interpretable facies.

5.2.Relevance of typology

The results show that the approach used in this work allows us to map the zonation of the mangrove only on spectral indices, acting as proxies of cover rate and stand height, but does not allow the extrapolation of information on species abundance for each class. These results are consistent with those of Lymburner et al. (2020), who obtained a three-class typology based on canopy openness (woodland (20-50%), open forest (50-80%), and closed forest (>80%)), using linear spectral unmixing. This typology allowed them to follow evolution over time, which is a future objective of this work.

However, our results suggest that the vegetation fraction per LSU is sensitive to mangrove seasonality. Therefore, the index can fluctuate without any changes in the canopy openness.

Therefore, following the evolution of classes with a known value amplitude and a quantified uncertainty will allow us to follow the intra-mangrove reorganization by reducing the errors of omissions and commissions of the changes.

Valderrama-Landeros et al. (2021) showed that typologies can be affected by mangrove phenology, and that certain dates of image acquisition are more conducive to the development of a reliable typology. In this study, we synthesized the phenological patterns of the classes and quantified the amplitude of their fluctuations over time, given the frequency of spectral similarities between classes during the year (Figure 8). Therefore, assessing changes in the future may be more appropriate, to apprehend signal breaks in the time series metrics of the mangrove rather than establishing a map with the same typology at each date. Indeed, the latter may be distorted by inter-annual climatic variability, which affects the spectral indices (Nicholson, 2013). In addition, Pastor-Guzman et al. (2018) showed that semi-arid mangroves with the same specific composition respond to the onset of the rainy season with a slight phenological delay that affects canopy reflectance values.

As was mentioned by Valderrama-Landeros et al. (2021), this could bias the classification of mangrove cover in areas with lower vegetation density. However, these authors showed that the period between the end of the dry season and beginning of the rainy season was the most favorable for producing accurate estimates of mangrove cover in Mexico. Our results indicated a slightly different optimal period. The end of the rainy season and beginning of the dry season showed the strongest contrasts between the classes on raw values and values modelled by harmonic regression. The climatic contexts of the two studies are similar; however, the 'inverse' character of Senegalese estuaries greatly influences salinity. A reduction in photosynthetic activity with increasing water salinity (George et al., 2020) or an impact on the seasonality of spectral indices (Celis-Hernandez et al., 2022) have been consistently observed. For Saloum, spectral contrasts appeared to be maximized when species faced lower salinities. Therefore, a typology based on objects that are more sensitive to spatial variations relative to neighboring pixels, rather than to fluctuations in pixel values, can partially overcome the constraints related to the phenology of mangroves mentioned above. Furthermore, the typology presented here and based on the annual phenological pattern allows us to follow the recommendations of Li et al. (2019) and Valderrama-Landeros et al. (2021) who advocate using images over a longer time series to potentially detect possible disturbances. For example, a similar typology has proven suitable for monitoring hurricane damage (Vizcaya-Martínez et al., 2022). Impacts of hydrological changes such as salinity could be monitored at least quarterly. This environmental parameter seems to be a major factor in the spatiotemporal dynamics of the Senegalese mangrove (Andrieu et al., 2020; Descroix et al., 2020; Lombard et al., 2020).

5.3.Perspectives: distinguishing stresses from disturbances

The choice of typology based on a 1-year time series is justified with a view to developing classes that are less sensitive to seasonal fluctuations. When mapping changes in mangrove zonation, we must distinguish between stress and disturbance, which both showed a lasting effect on zonation. The harmonic regression model allowed us to understand seasonal fluctuations and annual trends. Here, we used only the mean of the regression model values to classify the mangrove zonation. The amplitude (seasonal variability), phase (travel time from

the origin to the peak of the wave), and RMSE (non-seasonal variability) did not contribute to the robust detection of zonation. Nevertheless, these indicators could be of great importance for understanding the response of mangroves to environmental fluctuations. Celis-Hernandez et al. (2022) captured the impact of physicochemical variables on seasonal fluctuations of mangroves through phenological metrics. Nevertheless, as these authors pointed out, the long-term effects of fluctuations in physicochemical parameters are still poorly understood. Therefore, we suggest that future applications should focus on the impact of climatic variables and salinity on the spatial organization of mangroves at several temporal scales. We also recommend characterizing the impact of these variables and their fluctuations at several scales (spatial and temporal) on the possible threshold effects inducing mangrove dynamics at decadal scales. The use of long-term time series such as Landsat (Bullock et al., 2017; Pirasteh et al., 2021) could provide insights into mangrove responses with this typology over time. In this study, we quantified the uncertainty around plant fraction values to characterize potential changes in mangrove zonation. In the future, we recommend using change detection approaches from temporal segmentations, such as LandTrendR (Kennedy et al., 2010) or CCDC (Zhu and Woodcock, 2014). For example, LandTrendr has been successfully used for mangroves (de Jong et al., 2021). The uncertainty bounds identified in this work allow the parameters to be calibrated in a robust manner to effectively detect zonation changes. As was pointed out by Pasquarella et al. (2022), calibrating the sensitivity of these models to change detection is a key step in mapping land-cover changes.

6. Conclusion

Mapping mangrove zonation is challenging yet important in the management of this ecosystem. Plant formations are organized along environmental gradients, and therefore allow us to approximate the outcome of population dynamics processes that operate at a finer scale. Three homogeneous features were mapped at 10 m spatial resolution from Sentinel-1 and Sentinel-2 data. SAR and optical data have proved to be paramount for effective mangrove mapping. The vegetation fraction resulting from a linear spectral unmixing on optical data only allowed us to establish the following clustering: 'High riverine mangrove dominated by *Rhizophora racemosa'*, 'Low and dense mangrove with mixed *Rhizophora mangle* and *Avicennia germinans'*, 'Low and open mangrove with mixed *Rhizophora mangle* and *Avicennia germinans*'. The results of this study show that the average of the values of the plant fraction, obtained by harmonic regressions on each object, allows robust mapping of the zonation of the mangrove on the criteria of canopy cover and height of the stands. In addition, the temporal stability of the typology was assessed. The results indicated that an overall margin of error of 14.5% is expected if the plant formations are discriminated against the annual trend of the plant fraction. These acceptable results do not obscure the likelihood of confusion between the classes over time. This leads to probable commission errors and omissions regarding inter-annual zonation changes that must be addressed. Therefore, this study points out that low mangrove classes are most likely to be confused over time. Furthermore, from the perspective of mapping zonation changes on an inter-annual scale, the uncertainty bounds quantified in this study allowed us to estimate that the growth of dense mangrove stands can be reliably captured if the initial values of the low dense mangrove class increase between 16% and 45% for values between the 1st and 3rd quartiles. Conversely, a decrease in the height of the high mangrove stands while maintaining their density can be interpreted if a decrease of 10% to 20% of the vegetation fraction is observed. Second, a densification of the low mangrove canopy can be

855 interpreted if an increase of 13% to 28% in the vegetation fraction values was observed between
856 the 1st and 3rd quartile. Finally, an opening of the low mangrove could be observed if the
857 values of plant fraction of the initially dense mangrove decreased from 21% to 34% between
858 the 1st and 3rd quartile of the class. Therefore, these limits were intended to reliably identify
859 the response of mangrove zonation to environmental changes in the Saloum Delta. The
860 amplitudes of each zonation class identified in this study could allow the characterization and
861 distinction of stresses, disturbances, or recovery thresholds using temporal segmentation
862 methods.

863

Acknowledgments

We warmly thank Inssa Seydi for the many canoe trips, for having shared these observations with us for many years and for all the help provided in the field.

Funding details

This work was supported under grant IDEX UCA JEDI and by the CNRS UMR 7300 ESPACE

Disclosure statement

The authors declare that they have no known competing financial interests or personal relationships that could have appeared to influence the work reported in this paper.

Data availability statement

Publicly available datasets were analyzed in this study. This data can be found here: The original satellite data from Sentinel-1 and Sentinel-2 are publically accessible from the open cloud platform Google Earth Engine.

Sentinel-1 Data Link: https://developers.google.com/earth-engine/datasets/catalog/COPERNICUS_S1_GRD

Sentinel-2 Data Link: https://developers.google.com/earth-engine/datasets/catalog/COPERNICUS_S2_SR_HARMONIZED

The import of Sentinel-1 and Sentinel-2 data, the calculation of the number of images, the number of cloud-free pixels in the time series, and the harmonic model on the vegetation fraction derived from linear spectral unmixing are available in the following Google Earth Engine code : https://code.earthengine.google.com/29061ee4b48e419baf491180809e7530

The mangrove extent and zonation data products from this research project can be accessed through the following link: https://doi.org/10.34847/nkl.c7ecc507

Supplemental online material

Table: Significance of classes by p-value for the adopted typology based on height, canopy density and presence/absence of plant species.

HM: High mangrove – LDM: Low and dense mangrove - LOM: Low and open mangrove

a)

Canopy Cover

Class	p-value	p-value adjusted	significance
HM / LDM	0.011	0.021	*
HM / LOM	0.000456	0. 001	**
LDM / LOM	0. 016	0.021	*

b)

Height canopy

Class	p-value	p-value adjusted	significance
HM / LDM	0.002	0.005	**

	HM / LOM	0.0000138	0.0000414	****
	LDM / LOM	0.102	0.102	ns

c)

Rhizophora racemosa

Class	p-value	p-value adjusted	significance
HM / LDM	0.035	0.071	ns
HM / LOM	0.0000242	0.0000726	****
LDM / LOM	0.096	0.096	ns

d)

Rhizophora mangle

Class	p-value	p-value adjusted	significance
HM / LDM	0.864	1	ns
HM / LOM	0.807	1	ns
LDM / LOM	0.077	0.231	ns

e)

Avicennia germinans

Class	p-value	p-value adjusted	significance
HM / LDM	0.045	0.091	ns
HM / LOM	0.004	0.012	*
LDM / LOM	0.332	0.332	ns

References

R. Achanta and S. Süsstrunk. 2017. “Superpixels and Polygons Using Simple Non-Iterative Clustering.” In 2017 IEEE Conference on Computer Vision and Pattern Recognition (CVPR), 4895–4904. https://doi.org/10.1109/CVPR.2017.520.

Alonso, Alice, Rafael Muñoz-Carpena, Robert E. Kennedy, and Carolina Murcia. 2016. “Wetland Landscape Spatio-Temporal Degradation Dynamics Using the New Google Earth Engine Cloud-Based Platform: Opportunities for Non-Specialists in Remote Sensing.” Transactions of the ASABE 59 (5): 1331–42.

Andrieu, Julien. 2018. “Land Cover Changes on the West-African Coastline from the Saloum Delta (Senegal) to Rio Geba (Guinea-Bissau) between 1979 and 2015.” European Journal of Remote Sensing 51 (1): 314–25.

907 Andrieu, Julien, Florent Lombard, Ababacar Fall, Mamadou Thior, Boubacar Demba Ba, and
908 Barnabé Ephrem A. Dieme. 2020. “Botanical Field-Study and Remote Sensing to Describe
909 Mangrove Resilience in the Saloum Delta (Senegal) after 30 Years of Degradation Narrative.”
910 Forest Ecology and Management 461: 117963.

911 Andrieu, Julien. 2020. “Rice and Trees: Agrarian and Landscape Dynamics over 40 Years on
912 the Coast of Southern Senegal and The Gambia.” Dynamiques Environnementales. Journal
913 International de Géosciences et de l’environnement, no. 46: 2–23.

914 Arumugam, Manjula, Richard Niyomugabo, Farid Dahdouh-Guebas, and Jean Hugé. 2021.
915 “The Perceptions of Stakeholders on Current Management of Mangroves in the Sine-Saloum
916 Delta, Senegal.” Estuarine, Coastal and Shelf Science 248: 107160.
917 https://doi.org/10.1016/j.ecss.2020.107160.

918 Asenso Barnieh, Beatrice, Li Jia, Massimo Menenti, Jie Zhou, and Yelong Zeng. 2020.
919 “Mapping Land Use Land Cover Transitions at Different Spatiotemporal Scales in West
920 Africa.” Sustainability 12 (20).

921 Balke, Thorsten, Edward L. Webb, Eva van den Elzen, Demis Galli, Peter M. J. Herman, and
922 Tjeerd J. Bouma. 2013. “Seedling Establishment in a Dynamic Sedimentary Environment: A
923 Conceptual Framework Using Mangroves.” Journal of Applied Ecology 50 (3): 740–47.
924 https://doi.org/10.1111/1365-2664.12067.

925 Barusseau, J. P., E. H. S. Diop, and J. L. Saos. 1985. “Evidence of Dynamics Reversal in
926 Tropical Estuaries, Geomorphological and Sedimentological Consequences (Salum and
927 Casamance Rivers, Senegal).” Sedimentology 32 (4): 543–52. https://doi.org/10.1111/j.1365-
928 3091.1985.tb00469.x.

929 Belgiu, Mariana, and Lucian Drăguţ. 2016. “Random Forest in Remote Sensing: A Review of
930 Applications and Future Directions.” ISPRS Journal of Photogrammetry and Remote Sensing
931 114: 24–31.

932 Bivand, Roger, Micah Altman, Luc Anselin, Renato Assunção, Olaf Berke, Andrew Bernat,
933 and Guillaume Blanchet. 2015. “Package ‘Spdep.’” The Comprehensive R Archive Network.

934 Blaschke, Thomas, Stefan Lang, and Geoffrey Hay. 2008. Object-Based Image Analysis:
935 Spatial Concepts for Knowledge-Driven Remote Sensing Applications. Springer Science &
936 Business Media.

937 Blaschke, Thomas. 2010. “Object Based Image Analysis for Remote Sensing.” ISPRS Journal
938 of Photogrammetry and Remote Sensing 65 (1): 2–16.

939 Breiman, Leo. 2001. “Random Forests.” Machine Learning 45 (1): 5–32.

940 Bullock, Eric L., Sergio Fagherazzi, William Nardin, Phuoc Vo-Luong, Phong Nguyen, and
941 Curtis E. Woodcock. 2017. “Temporal Patterns in Species Zonation in a Mangrove Forest in
942 the Mekong Delta, Vietnam, Using a Time Series of Landsat Imagery.” Continental Shelf
943 Research 147: 144–54.

944 Bullock, Eric L., Curtis E. Woodcock, and Pontus Olofsson. 2020. “Monitoring Tropical Forest
945 Degradation Using Spectral Unmixing and Landsat Time Series Analysis.” Remote Sensing of
946 Environment 238: 110968.

947 Bunting, Pete, Ake Rosenqvist, Richard M. Lucas, Lisa-Maria Rebelo, Lammert Hilarides,
948 Nathan Thomas, Andy Hardy, Takuya Itoh, Masanobu Shimada, and C. Max Finlayson. 2018.
949 "The Global Mangrove Watch—A New 2010 Global Baseline of Mangrove Extent" Remote
950 Sensing 10, no. 10: 1669. https://doi.org/10.3390/rs10101669

951 Cabral, Ana I. R., and Fernando Lagos Costa. 2017. "Land Cover Changes and Landscape
952 Pattern Dynamics in Senegal and Guinea Bissau Borderland." Applied Geography 82: 115–28.
953 https://doi.org/10.1016/j.apgeog.2017.03.010.

954 Cárdenas, Nicolás Younes, Karen E. Joyce, and Stefan W. Maier. 2017. "Monitoring Mangrove
955 Forests: Are We Taking Full Advantage of Technology?" International Journal of Applied
956 Earth Observation and Geoinformation 63: 1–14.

957 Celis-Hernandez, Omar, Miguel Villoslada-Peciña, Raymond D. Ward, T.F. Bergamo, Rosela
958 Perez-Ceballos, and María Patricia Girón-García. 2022. "Impacts of Environmental Pollution
959 on Mangrove Phenology: Combining Remotely Sensed Data and Generalized Additive
960 Models." Science of The Total Environment 810 (March): 152309.
961 https://doi.org/10.1016/j.scitotenv.2021.152309.

962 Chen, Bangqian, Xiangming Xiao, Xiangping Li, Lianghao Pan, Russell Doughty, Jun Ma,
963 Jinwei Dong, Yuanwei Qin, Bin Zhao, and Zhixiang Wu. 2017. "A Mangrove Forest Map of
964 China in 2015: Analysis of Time Series Landsat 7/8 and Sentinel-1A Imagery in Google Earth
965 Engine Cloud Computing Platform." ISPRS Journal of Photogrammetry and Remote Sensing
966 131: 104–20.

967 Chen, Na. 2020. "Mapping Mangrove in Dongzhaigang, China Using Sentinel-2 Imagery."
968 Journal of Applied Remote Sensing 14 (1): 014508.

969 Chen, Na. 2020. "Mapping Mangrove in Dongzhaigang, China Using Sentinel-2 Imagery."
970 Journal of Applied Remote Sensing 14 (1): 014508.

971 Conchedda, Giulia, Laurent Durieux, and Philippe Mayaux. 2008. "An Object-Based Method
972 for Mapping and Change Analysis in Mangrove Ecosystems." Theme Issue: Remote Sensing
973 of the Coastal Ecosystems 63 (5): 578–89. https://doi.org/10.1016/j.isprsjprs.2008.04.002.

974 Conchedda, Giulia, Eric F. Lambin, and Philippe Mayaux. 2011. "Between land and sea:
975 livelihoods and environmental changes in mangrove ecosystems of Senegal." Annals of the
976 Association of American Geographers 101, no. 6 1259-1284.

977 Cormier-Salem, Marie-Christine. 1999. "Rivières du Sud." Sociétés et mangroves ouest-
978 africaines 1: 2.

979 Cormier-Salem, Marie-Christine, and J. Panfili. 2016. "Mangrove reforestation: greening or
980 grabbing coastal zones and deltas? Case studies in Senegal." African Journal of Aquatic
981 Science 41, no. 1 :89-98.

982 Clinton, N. 2016. "Time Series Analysis in Earth Engine."

983 Jong, Steven M. de, Youchen Shen, Job de Vries, Ginny Bijnaar, Barend van Maanen, Pieter
984 Augustinus, and Pita Verweij. 2021. "Mapping Mangrove Dynamics and Colonization Patterns
985 at the Suriname Coast Using Historic Satellite Data and the LandTrendr Algorithm."

International Journal of Applied Earth Observation and Geoinformation 97 (May) : 102293. https://doi.org/10.1016/j.jag.2020.102293.

Descroix, Luc, Aïda Diongue Niang, Gérémy Panthou, Ansoumana Bodian, Youssouph Sane, Honoré Dacosta, Moussa Malam Abdou, Jean-Pierre Vandervaere, and Guillaume Quantin. 2015. “Évolution Récente de La Pluviométrie En Afrique de l’ouest à Travers Deux Régions : La Sénégambie et Le Bassin Du Niger Moyen.” Climatologie 12: 25–43. https://doi.org/10.4267/climatologie.1105.

Luc Descroix. 2018. Processus et enjeux d'eau en Afrique de l'Ouest soudano-sahélienne. EAC, 320 p.

Descroix, Luc, Yancouba Sané, Mamadou Thior, Sylvie-Paméla Manga, Boubacar D. Ba, Joseph Mingou, Victor Mendy, et al. 2020. “Inverse Estuaries in West Africa: Evidence of the Rainfall Recovery?” Water 12 (3). https://doi.org/10.3390/w12030647.

Díaz-Uriarte, Ramón, and Sara Alvarez de Andrés. 2006. "Gene selection and classification of microarray data using random forest." BMC bioinformatics 7, no. 1, 1-13.

Balla Dieye, E. L., Amadou Tahirou Diaw, Tidiane Sané, and Ngor Ndour. 2013. "Dynamique de la mangrove de l’estuaire du Saloum (Sénégal) entre 1972 et 2010." Cybergeo: European Journal of Geography.

Diop, E.S. 1990. La côte Ouest-Africaine: du Saloum (Senegal). à la Mellacoree (Rep de Guinee). Collection Études et Thé ses, Éditions de l’ORSTOM, 2 volumes; Paris, 379 pp.

Diop, E.S., A. Soumare, N. Diallo, and A. Guisse. 1997. “Recent Changes of the Mangroves of the Saloum River Estuary, Senegal.” Mangroves and Salt Marshes 1 (3): 163–72. https://doi.org/10.1023/A:1009900724172.

Drăguţ, Lucian, Dirk Tiede, and Shaun R. Levick. 2010. “ESP: A Tool to Estimate Scale Parameter for Multiresolution Image Segmentation of Remotely Sensed Data.” International Journal of Geographical Information Science 24 (6): 859–71. https://doi.org/10.1080/13658810903174803.

Drăguţ, L., O. Csillik, C. Eisank, and D. Tiede. 2014. “Automated Parameterisation for Multi-Scale Image Segmentation on Multiple Layers.” ISPRS Journal of Photogrammetry and Remote Sensing 88 (February): 119–27. https://doi.org/10.1016/j.isprsjprs.2013.11.018.

Dronova, Iryna. 2015. “Object-Based Image Analysis in Wetland Research: A Review.” Remote Sensing 7 (5): 6380–6413. https://doi.org/10.3390/rs70506380.

Espindola, G. M., G. Camara, I. A. Reis, L. S. Bins, and A. M. Monteiro. 2006. “Parameter Selection for Region-growing Image Segmentation Algorithms Using Spatial Autocorrelation.” International Journal of Remote Sensing 27 (14): 3035–40. https://doi.org/10.1080/01431160600617194.

Fent, Ashley, Rémi Bardou, Judith Carney, and Kyle Cavanaugh. 2019. “Transborder Political Ecology of Mangroves in Senegal and The Gambia.” Global Environmental Change 54 (January): 214–26.

Francisco Flores De Santiago, John M. Kovacs & Patrick Lafrance. 2013. An object-oriented classification method for mapping mangroves in Guinea, West Africa, using multipolarized ALOS PALSAR L-band data, International Journal of Remote Sensing, 34:2, 563-586, DOI: 10.1080/01431161.2012.715773

Gao, Bo-cai. 1996. "NDWI—A Normalized Difference Water Index for Remote Sensing of Vegetation Liquid Water from Space." Remote Sensing of Environment 58 (3): 257–66. https://doi.org/10.1016/S0034-4257(96)00067-3.

George, Rajee, Hitendra Padalia, S. K. Sinha, and A. Senthil Kumar. 2020. "Evaluating Sensitivity of Hyperspectral Indices for Estimating Mangrove Chlorophyll in Middle Andaman Island, India." Environmental Monitoring and Assessment 191 (3): 785. https://doi.org/10.1007/s10661-019-7679-6.

Ghazali, Mochamad Firman, and Ketut WIkantika. 2021. "Pre-Assessment of the Potential of Dual Polarization of Sentinel 1 Data for Mapping the Mangrove Tree Species Distribution in South Bali, Indonesia." In 2021 7th Asia-Pacific Conference on Synthetic Aperture Radar (APSAR), 1–6. https://doi.org/10.1109/APSAR52370.2021.9688441.

Giri, C., E. Ochieng, L. L. Tieszen, Z. Zhu, A. Singh, T. Loveland, J. Masek, and N. Duke. 2011. "Status and Distribution of Mangrove Forests of the World Using Earth Observation Satellite Data." Global Ecology and Biogeography 20 (1): 154–59. https://doi.org/10.1111/j.1466-8238.2010.00584.x.

Giri, Chandra, Jordan Long, Sawaid Abbas, R.Mani Murali, Faisal M. Qamer, Bruce Pengra, and David Thau. 2015. "Distribution and Dynamics of Mangrove Forests of South Asia." Land Cover/Land Use Change (LC/LUC) and Environmental Impacts in South Asia 148 (January): 101–11. https://doi.org/10.1016/j.jenvman.2014.01.020.

Gorelick, Noel, Matt Hancher, Mike Dixon, Simon Ilyushchenko, David Thau, and Rebecca Moore. 2017. "Google Earth Engine : Planetary-Scale Geospatial Analysis for Everyone." Big Remotely Sensed Data : Tools, Applications and 39xpériences 202 (December) : 18–27. https://doi.org/10.1016/j.rse.2017.06.031.

Gudex-Cross, David, Jennifer Pontius, and Alison Adams. 2017. "Enhanced Forest Cover Mapping Using Spectral Unmixing and Object-Based Classification of Multi-Temporal Landsat Imagery." Remote Sensing of Environment 196 (July): 193–204.

Gupta, Kaushik, Anirban Mukhopadhyay, Sandip Giri, Abhra Chanda, Sayani Datta Majumdar, Sourav Samanta, Debasish Mitra, Rabindro N. Samal, Ajit K. Pattnaik, and Sugata Hazra. 2018. "An Index for Discrimination of Mangroves from Non-Mangroves Using LANDSAT 8 OLI Imagery." MethodsX 5 (January): 1129–39. https://doi.org/10.1016/j.mex.2018.09.011.

Han, Xingxing, Lian Feng, Chuanmin Hu, and Philip Kramer. 2018. "Hurricane-Induced Changes in the Everglades National Park Mangrove Forest: Landsat Observations Between 1985 and 2017." Journal of Geophysical Research: Biogeosciences 123 (11): 3470–88. https://doi.org/10.1029/2018JG004501.

Haralick, Robert M., K. Shanmugam, and Its'Hak Dinstein. 1973. "Textural Features for Image Classification." IEEE Transactions on Systems, Man, and Cybernetics SMC-3 (6): 610–21. https://doi.org/10.1109/TSMC.1973.4309314.

Hossain, Mohammad D., and Dongmei Chen. 2019. "Segmentation for Object-Based Image Analysis (OBIA): A Review of Algorithms and Challenges from Remote Sensing Perspective." ISPRS Journal of Photogrammetry and Remote Sensing 150 (April): 115–34. https://doi.org/10.1016/j.isprsjprs.2019.02.009.

Hu, Qiong, Damien Sulla-Menashe, Baodong Xu, He Yin, Huajun Tang, Peng Yang, and Wenbin Wu. 2019. "A Phenology-Based Spectral and Temporal Feature Selection Method for Crop Mapping from Satellite Time Series." International Journal of Applied Earth Observation and Geoinformation 80: 218–29. https://doi.org/10.1016/j.jag.2019.04.014.

Jakubauskas, Mark E., David R. Legates, and Jude H. Kastens. 2002. "Crop Identification Using Harmonic Analysis of Time-Series AVHRR NDVI Data." Computers and Electronics in Agriculture 37 (1): 127–39. https://doi.org/10.1016/S0168-1699(02)00116-3.

Jia, Mingming, Zongming Wang, Yuanzhi Zhang, Dehua Mao, and Chao Wang. 2018. "Monitoring Loss and Recovery of Mangrove Forests during 42 Years: The Achievements of Mangrove Conservation in China." International Journal of Applied Earth Observation and Geoinformation 73 (December): 535–45. https://doi.org/10.1016/j.jag.2018.07.025.

Jia, Mingming, Zongming Wang, Dehua Mao, Chunying Ren, Chao Wang, and Yeqiao Wang. 2021. "Rapid, Robust, and Automated Mapping of Tidal Flats in China Using Time Series Sentinel-2 Images and Google Earth Engine." Remote Sensing of Environment 255 (March): 112285. https://doi.org/10.1016/j.rse.2021.112285.

Jia, Mingming, Zongming Wang, Dehua Mao, Chunying Ren, Chao Wang, and Yeqiao Wang. 2021. "Rapid, Robust, and Automated Mapping of Tidal Flats in China Using Time Series Sentinel-2 Images and Google Earth Engine." Remote Sensing of Environment 255 (March): 112285. https://doi.org/10.1016/j.rse.2021.112285.

Johnson, Brian, and Zhixiao Xie. 2011. "Unsupervised Image Segmentation Evaluation and Refinement Using a Multi-Scale Approach." ISPRS Journal of Photogrammetry and Remote Sensing 66 (4): 473–83. https://doi.org/10.1016/j.isprsjprs.2011.02.006.

Johnson, Brian A., Milben Bragais, Isao Endo, Damasa B. Magcale-Macandog, and Paula Beatrice M. Macandog. 2015. "Image Segmentation Parameter Optimization Considering Within- and Between-Segment Heterogeneity at Multiple Scale Levels: Test Case for Mapping Residential Areas Using Landsat Imagery." ISPRS International Journal of Geo-Information 4 (4). .

Kennedy, Robert E., Zhiqiang Yang, and Warren B. Cohen. 2010. "Detecting Trends in Forest Disturbance and Recovery Using Yearly Landsat Time Series : 1. LandTrendr — Temporal Segmentation Algorithms." Remote Sensing of Environment 114 (12) : 2897–2910.

Kuenzer, Claudia, Andrea Bluemel, Steffen Gebhardt, Tuan Vo Quoc, and Stefan Dech. 2011. "Remote Sensing of Mangrove Ecosystems: A Review" Remote Sensing 3, no. 5: 878-928. https://doi.org/10.3390/rs3050878

1103 Krauss, Ken W., Catherine E. Lovelock, Karen L. McKee, Laura López-Hoffman, Sharon M.L.
1104 Ewe, and Wayne P. Sousa. 2008. "Environmental Drivers in Mangrove Establishment and
1105 Early Development: A Review." Mangrove Ecology – Applications in Forestry and Costal
1106 Zone Management 89 (2): 105–27. https://doi.org/10.1016/j.aquabot.2007.12.014.

1107 Li, Xianju, Weitao Chen, Xinwen Cheng, and Lizhe Wang. 2016. "A Comparison of Machine
1108 Learning Algorithms for Mapping of Complex Surface-Mined and Agricultural Landscapes
1109 Using ZiYuan-3 Stereo Satellite Imagery." Remote Sensing 8 (6).
1110 https://doi.org/10.3390/rs8060514.

1111 Li, Huiying, Mingming Jia, Rong Zhang, Yongxing Ren, and Xin Wen. 2019. "Incorporating
1112 the Plant Phenological Trajectory into Mangrove Species Mapping with Dense Time Series
1113 Sentinel-2 Imagery and the Google Earth Engine Platform." Remote Sensing 11 (21).
1114 https://doi.org/10.3390/rs11212479.

1115 Liu, Xue, Temilola E. Fatoyinbo, Nathan M. Thomas, Weihe Wendy Guan, Yanni Zhan, Pinki
1116 Mondal, David Lagomasino, et al. 2021. "Large-Scale High-Resolution Coastal Mangrove
1117 Forests Mapping Across West Africa With Machine Learning Ensemble and Satellite Big
1118 Data." Frontiers in Earth Science 8.
1119 https://www.frontiersin.org/articles/10.3389/feart.2020.560933.

1120 Lu, Ying, and Le Wang. 2021. "How to Automate Timely Large-Scale Mangrove Mapping
1121 with Remote Sensing." Remote Sensing of Environment 264 (October): 112584.
1122 https://doi.org/10.1016/j.rse.2021.112584.

1123 Lombard, Florent, and Andrieu Julien. 2021. "Mapping Mangrove Zonation Changes in
1124 Senegal with Landsat Imagery Using an OBIA Approach Combined with Linear Spectral
1125 Unmixing." Remote Sensing 13 (10). https://doi.org/10.3390/rs13101961.

1126 Lombard, Florent, Andrieu Julien, and Descroix Luc. 2021. "La Population d'Avicennia
1127 Germinans Du Delta Du Saloum Est-Elle Relictuelle Depuis La Dernière Période Humide ?"
1128 BOIS & FORETS DES TROPIQUES 346 (0): 51–64.
1129 https://doi.org/10.19182/bft2020.346.a36296.

1130 Lymburner, Leo, Peter Bunting, Richard Lucas, Peter Scarth, Imam Alam, Claire Phillips,
1131 Catherine Ticehurst, and Alex Held. 2020. "Mapping the Multi-Decadal Mangrove Dynamics
1132 of the Australian Coastline." Time Series Analysis with High Spatial Resolution Imagery 238
1133 (March): 111185. https://doi.org/10.1016/j.rse.2019.05.004.

1134 Ma, Lei, Manchun Li, Xiaoxue Ma, Liang Cheng, Peijun Du, and Yongxue Liu. 2017. "A
1135 Review of Supervised Object-Based Land-Cover Image Classification." ISPRS Journal of
1136 Photogrammetry and Remote Sensing 130: 277–93.
1137 https://doi.org/10.1016/j.isprsjprs.2017.06.001.

1138 Marius, Claude. 1985. Mangroves du Sénégal et de la Gambie : écologie, pédologie, géochimie,
1139 mise en valeur et aménagement. Travaux et Documents de l'ORSTOM. Paris: ORSTOM.
1140 https://www.documentation.ird.fr/hor/fdi:19338.

1141 McFEETERS, S. K. 1996. "The Use of the Normalized Difference Water Index (NDWI) in the
1142 Delineation of Open Water Features." International Journal of Remote Sensing 17 (7): 1425–
1143 32. https://doi.org/10.1080/01431169608948714.

1144 Midekisa, Alemayehu, Felix Holl, David J. Savory, Ricardo Andrade-Pacheco, Peter W.
1145 Gething, Adam Bennett, and Hugh J. W. Sturrock. 2017. “Mapping Land Cover Change over
1146 Continental Africa Using Landsat and Google Earth Engine Cloud Computing.” PLOS ONE
1147 12 (9): e0184926. https://doi.org/10.1371/journal.pone.0184926.

1148 Mondal, Pinki, Xue Liu, Temilola E. Fatoyinbo, and David Lagomasino. 2019. “Evaluating
1149 Combinations of Sentinel-2 Data and Machine-Learning Algorithms for Mangrove Mapping
1150 in West Africa.” Remote Sensing 11 (24). https://doi.org/10.3390/rs11242928.

1151 Monsef, Hesham Abd-El, and Scot E. Smith. 2017. “A New Approach for Estimating
1152 Mangrove Canopy Cover Using Landsat 8 Imagery.” Computers and Electronics in Agriculture
1153 135 (April): 183–94. https://doi.org/10.1016/j.compag.2017.02.007.

1154 Mukherjee, Nibedita, William J. Sutherland, Lynn Dicks, Jean Hugé, Nico Koedam, and Farid
1155 Dahdouh-Guebas. 2014. “Ecosystem Service Valuations of Mangrove Ecosystems to Inform
1156 Decision Making and Future Valuation Exercises.” PLOS ONE 9 (9): e107706.
1157 https://doi.org/10.1371/journal.pone.0107706.

1158 Mutanga, Onisimo, and Lalit Kumar. 2019. “Google Earth Engine Applications.” Remote
1159 Sensing 11 (5). https://doi.org/10.3390/rs11050591.

1160 Myint, Soe W., Chandra P. Giri, Le Wang, Zhiliang Zhu, and Shana C. Gillette. 2008.
1161 “Identifying Mangrove Species and Their Surrounding Land Use and Land Cover Classes
1162 Using an Object-Oriented Approach with a Lacunarity Spatial Measure.” GIScience & Remote
1163 Sensing 45 (2): 188–208. https://doi.org/10.2747/1548-1603.45.2.188.

1164 Myint, Soe W., Patricia Gober, Anthony Brazel, Susanne Grossman-Clarke, and Qihao Weng.
1165 2011. “Per-Pixel vs. Object-Based Classification of Urban Land Cover Extraction Using High
1166 Spatial Resolution Imagery.” Remote Sensing of Environment 115 (5) : 1145–61.
1167 https://doi.org/10.1016/j.rse.2010.12.017.

1168 Ndour, Ngor, Sara Danièle Dieng, and Mamadou Fall. 2012. “Rôles Des Mangroves, Modes
1169 et Perspectives de Gestion Au Delta Du Saloum (Sénégal).” VertigO - la revue électronique en
1170 sciences de l'environnement, Volume 11 Numéro 3 | décembre 2011. DOI :
1171 https://doi.org/10.4000/vertigo.11515

1172 Nicholson, Sharon E. 2013. “The West African Sahel: A Review of Recent Studies on the
1173 Rainfall Regime and Its Interannual Variability.” Edited by D.-Y. Wang, I. Bordi, and F. Acs.
1174 ISRN Meteorology 2013 (February): 453521. https://doi.org/10.1155/2013/453521.

1175 Olofsson, Pontus, Giles M. Foody, Martin Herold, Stephen V. Stehman, Curtis E. Woodcock,
1176 and Michael A. Wulder. 2014. “Good Practices for Estimating Area and Assessing Accuracy
1177 of Land Change.” Remote Sensing of Environment 148: 42–57.
1178 https://doi.org/10.1016/j.rse.2014.02.015.

1179 Pasquarella, Valerie J., Christopher E. Holden, and Curtis E. Woodcock. 2018. “Improved
1180 Mapping of Forest Type Using Spectral-Temporal Landsat Features.” Remote Sensing of
1181 Environment 210: 193–207. https://doi.org/10.1016/j.rse.2018.02.064.

1182 Pasquarella, Valerie J., Paulo Arévalo, Kelsee H. Bratley, Eric L. Bullock, Noel Gorelick,
1183 Zhiqiang Yang, and Robert E. Kennedy. 2022. “Demystifying LandTrendr and CCDC

Temporal Segmentation." International Journal of Applied Earth Observation and Geoinformation 110 (June): 102806. https://doi.org/10.1016/j.jag.2022.102806.

Pastor-Guzman, J., Jadunandan Dash, and Peter M. Atkinson. 2018. "Remote Sensing of Mangrove Forest Phenology and Its Environmental Drivers." Remote Sensing of Environment 205 (February): 71–84. https://doi.org/10.1016/j.rse.2017.11.009.

Pirasteh, Saied, Eric K. Zenner, Davood Mafi-Gholami, Abolfazl Jaafari, Akram Nouri Kamari, Guoxiang Liu, Qing Zhu, and Jonathan Li. 2021. "Modeling Mangrove Responses to Multi-Decadal Climate Change and Anthropogenic Impacts Using a Long-Term Time Series of Satellite Imagery." International Journal of Applied Earth Observation and Geoinformation 102: 102390.

Rasul, Azad, Heiko Balzter, Gaylan R. Faqe Ibrahim, Hasan M. Hameed, James Wheeler, Bashir Adamu, Sa'ad Ibrahim, and Peshawa M. Najmaddin. 2018. "Applying Built-Up and Bare-Soil Indices from Landsat 8 to Cities in Dry Climates" Land 7, no. 3: 81. https://doi.org/10.3390/land7030081

Rouse, Jr., J. W., R. H. Haas, J. A. Schell, and D. W. Deering. 1974. "Monitoring Vegetation Systems in the Great Plains with Erts." In NASA Special Publication, 351:309.

Schulz, Dario, He Yin, Bernhard Tischbein, Sarah Verleysdonk, Rabani Adamou, and Navneet Kumar. 2021. "Land Use Mapping Using Sentinel-1 and Sentinel-2 Time Series in a Heterogeneous Landscape in Niger, Sahel." ISPRS Journal of Photogrammetry and Remote Sensing 178: 97–111. https://doi.org/10.1016/j.isprsjprs.2021.06.005.

Sow, M., Diallo, A., Diallo, N., Dixon, C. A., & Guissé, A. 1991. Formations végétales et sols dans les mangroves des Rivières du Sud. In Cormier-Salem, M. (Ed.), Dynamique et usages de la mangrove dans les pays des rivières du Sud, du Sénégal à la Sierra Leone. IRD Éditions. doi:10.4000/books.irdeditions.3690

Speiser, Jaime Lynn, Michael E. Miller, Janet Tooze, and Edward Ip. 2019. "A Comparison of Random Forest Variable Selection Methods for Classification Prediction Modeling." Expert Systems with Applications 134: 93–101. https://doi.org/10.1016/j.eswa.2019.05.028.

Stehman, Stephen V. 1997. "Selecting and Interpreting Measures of Thematic Classification Accuracy." Remote Sensing of Environment 62 (1): 77–89. https://doi.org/10.1016/S0034-4257(97)00083-7.

Stromann, Oliver, Andrea Nascetti, Osama Yousif, and Yifang Ban. 2020. "Dimensionality Reduction and Feature Selection for Object-Based Land Cover Classification Based on Sentinel-1 and Sentinel-2 Time Series Using Google Earth Engine." Remote Sensing 12 (1). https://doi.org/10.3390/rs12010076.

Taureau, Florent, Marc Robin, Christophe Proisy, François Fromard, Daniel Imbert, and Françoise Debaine. 2019. "Mapping the Mangrove Forest Canopy Using Spectral Unmixing of Very High Spatial Resolution Satellite Images." Remote Sensing 11 (3). https://doi.org/10.3390/rs11030367.

Temudo, Marina Padrão, Rui Figueira, and Manuel Abrantes. 2015. "Landscapes of Bio-Cultural Diversity: Shifting Cultivation in Guinea-Bissau, West Africa." Agroforestry Systems 89 (1): 175–91. https://doi.org/10.1007/s10457-014-9752-z.

Valderrama-Landeros, L., F. Flores-de-Santiago, J. M. Kovacs, and F. Flores-Verdugo. 2018. "An Assessment of Commonly Employed Satellite-Based Remote Sensors for Mapping Mangrove Species in Mexico Using an NDVI-Based Classification Scheme." Environmental Monitoring and Assessment 190 (1): 23. https://doi.org/10.1007/s10661-017-6399-z.

Valderrama-Landeros, Luis, Francisco Flores-Verdugo, Ranulfo Rodríguez-Sobreyra, John M. Kovacs, and Francisco Flores-de-Santiago. 2021. "Extrapolating Canopy Phenology Information Using Sentinel-2 Data and the Google Earth Engine Platform to Identify the Optimal Dates for Remotely Sensed Image Acquisition of Semiarid Mangroves." Journal of Environmental Management 279 (February) : 111617. https://doi.org/10.1016/j.jenvman.2020.111617.

Vizcaya-Martínez, Diego Arturo, Francisco Flores-de-Santiago, Luis Valderrama-Landeros, David Serrano, Ranulfo Rodríguez-Sobreyra, León Felipe Álvarez-Sánchez, and Francisco Flores-Verdugo. 2022. "Monitoring Detailed Mangrove Hurricane Damage and Early Recovery Using Multisource Remote Sensing Data." Journal of Environmental Management 320 (October): 115830. https://doi.org/10.1016/j.jenvman.2022.115830.

Walters, Bradley B., Patrik Rönnbäck, John M. Kovacs, Beatrice Crona, Syed Ainul Hussain, Ruchi Badola, Jurgenne H. Primavera, Edward Barbier, and Farid Dahdouh-Guebas. 2008. "Ethnobiology, Socio-Economics and Management of Mangrove Forests: A Review." Mangrove Ecology – Applications in Forestry and Costal Zone Management 89 (2): 220–36. https://doi.org/10.1016/j.aquabot.2008.02.009.

Wang, Dezhi, Bo Wan, Penghua Qiu, Yanjun Su, Qinghua Guo, Run Wang, Fei Sun, and Xincai Wu. 2018. "Evaluating the Performance of Sentinel-2, Landsat 8 and Pléiades-1 in Mapping Mangrove Extent and Species." Remote Sensing 10 (9). https://doi.org/10.3390/rs10091468.

Wang, Le, Mingming Jia, Dameng Yin, and Jinyan Tian. 2019. "A Review of Remote Sensing for Mangrove Forests: 1956–2018." Remote Sensing of Environment 231 (September): 111223. https://doi.org/10.1016/j.rse.2019.111223.

Wang, Xiaona, Le Wang, Jinyan Tian, and Chen Shi. 2021. "Object-Based Spectral-Phenological Features for Mapping Invasive Spartina Alterniflora." International Journal of Applied Earth Observation and Geoinformation 101: 102349. https://doi.org/10.1016/j.jag.2021.102349.

Xiao, Han, Fenzhen Su, Dongjie Fu, Vincent Lyne, Gaohuan Liu, Tingting Pan, and Jiakun Teng. 2021. "Optimal and Robust Vegetation Mapping in Complex Environments Using Multiple Satellite Imagery: Application to Mangroves in Southeast Asia." International Journal of Applied Earth Observation and Geoinformation 99: 102320. https://doi.org/10.1016/j.jag.2021.102320.

Zanaga, Daniele, Ruben Van De Kerchove, Wanda De Keersmaecker, Niels Souverijns, Carsten Brockmann, Ralf Quast, Jan Wevers, et al. 2021. "ESA WorldCover 10 m 2020 V100." VITO. https://edepot.wur.nl/576022.

Zhang, Xuehong, Paul M. Treitz, Dongmei Chen, Chang Quan, Lixin Shi, and Xinhui Li. 2017. "Mapping Mangrove Forests Using Multi-Tidal Remotely-Sensed Data and a Decision-Tree-

Based Procedure." International Journal of Applied Earth Observation and Geoinformation 62 (October): 201–14. https://doi.org/10.1016/j.jag.2017.06.010.

Zhao, Chuanpeng, and Cheng-Zhi Qin. 2020. "10-m-Resolution Mangrove Maps of China Derived from Multi-Source and Multi-Temporal Satellite Observations." ISPRS Journal of Photogrammetry and Remote Sensing 169 (November): 389–405. https://doi.org/10.1016/j.isprsjprs.2020.10.001.

Zhu, Zhe, and Curtis E. Woodcock. 2014. "Continuous Change Detection and Classification of Land Cover Using All Available Landsat Data." Remote Sensing of Environment 144: 152–71. https://doi.org/10.1016/j.rse.2014.01.011.